Numerical simulations of core-annular flow through a horizontal pipe

S.A. Konings

December, 2017

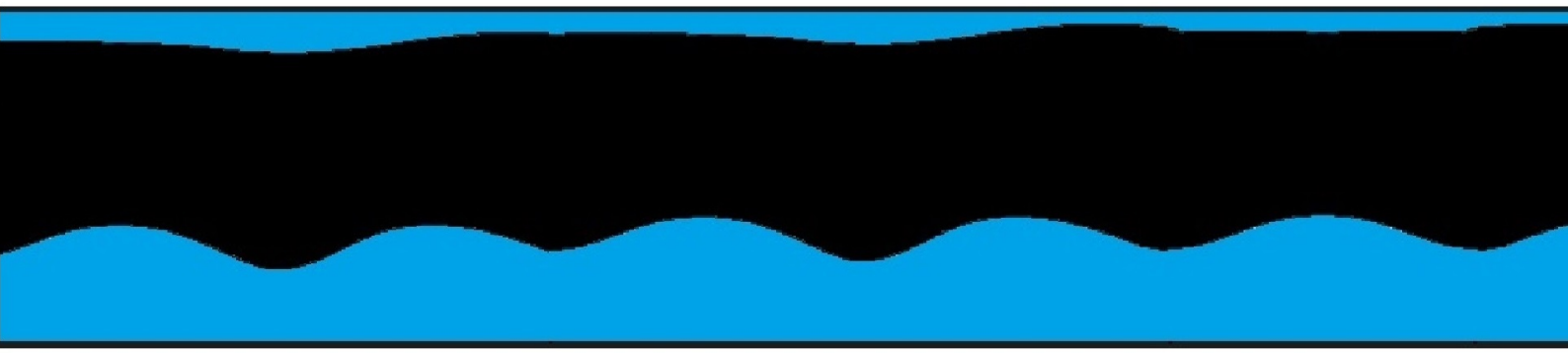

Master of Science
Mechanical Engineering

TU Delft Delft University of Technology

Challenge the future

Numerical simulations of core-annular flow through a horizontal pipe

by

S.A. Konings

in partial fulfillment of the requirements for the degree of

Master of Science
in Mechanical Engineering

at the Delft University of Technology,
to be defended publicly on Tuesday December 12, 2017 at 13:30 AM.

Supervisor:	Prof. dr. ir. R.A.W.M. Henkes,	TU Delft
	Prof. dr. ir. G. Ooms,	TU Delft
	dr. ir. M.J.B.M. Pourquie,	TU Delft
Thesis committee:	dr. S. Kenjeres,	TU Delft

TU Delft Delft University of Technology

Preface

Over the last year I found out how interesting and challenging a small rectangular picture with two different colors can be. It reminds me of art, which the phenomenon of core-annular flow actually also is. Core-annular flow is a very fascinating topic to work on and has introduced me to the interesting area of multiphase flow and has further improved my numerical skills.

I would like to express my sincere appreciation to the people who helped me accomplishing the work described in this report. Matheui Pourquie for all detailed explanations to all my questions. Ruud Henkes for the good feedback during the progress meetings, and the valuable help with writing the report. Gijs Ooms for all the help and mainly for conveying his enthusiasm on the subject of core-annular flow. And as last, but certainly not least, my dearest Leonoor for all the social support.

Swen Alexander Konings
Delft, December 2017

Abstract

Core-annular flow is an efficient flow regime for the transportation of viscous oils. The viscous oil in the core is surrounded and lubricated with an annulus of water. Water has a low viscosity and therefore reduces the pressure drop. Numerical simulations are performed for horizontal core-annular flow by using the Volume of fluid (VOF) method to solve the Reynolds-averaged Navier-Stokes equations (RANS) in OpenFOAM. Periodic boundary conditions are used for a small pipe section. With periodic boundary conditions the maximum wavelength at the oil-water interface is imposed together with the oil and water holdup fractions.

Numerical results are compared with recent experimental data. Oil viscosities between 3338 cSt at 20°C and 383 cSt at 50°C are solved with a fixed total flow rate. The 20°C simulation converged to the desired water cut of 20%, similar to the experiment. At this 20% water cut a comparable pressure gradient is found with the experiment. At higher temperatures (i.e. lower viscosities) deviations from the desired water cut of 20% are obtained. The different water cut values lead to differences between the numerical and experimental pressure gradients.

Additional simulations are carried out for the oil viscosity of 718 cSt at 40°C. Instead of a fixed total flow rate these simulations are solved with a fixed pressure gradient. This solving method is found to be considerable faster. Different holdup fractions and pressure gradients are imposed which resulted in different water cut and flow rate values. Numerical results are interpolated for the experimental water cut values of 9%, 12% and 15% at similar flow rates. Differences of 98%, 24% and 37% are found for the water cut of 9%, 12% and 15% respectively. An interpolation is not possible for the experimental water cut of 20% as this experiment is outside the covered solution region of the numerical results. This difference is caused due to an incorrectly used domain length.

The study is finished with holdup estimations of the experiments. Flow visualizations from a high speed camera are used which are made during the experiments. Oil holdup fractions of 0.749 are found for a water cut of 20%. This holdup fraction corresponds exactly with the imposed holdup fraction for the different viscosity simulations which are solves with the fixed total flow rate. Only the 3338 cSt at 20°C converged, however, to the water cut of 20%. ’

Contents

List of Figures

List of Tables

List of Symbols

ϵ	Turbulent dissipation	[m^2/s^3]
ϵ_w	Water cut	[-]
μ	Dynamic viscosity	[kg/(m·s)]
μ_t	Turbulent eddy viscosity	[kg/(m·s)]
ν	Kinematic viscosity	[cSt]
ρ	Density	[kg/m^3]
σ	Surface tension	[N/m]
τ_w	Wall shear stress	[Pa]
A	Area	[m^2]
A^*	Scaled amplitude size	[-]
Co	Courant number	[-]
H	Phase holdup	[-]
h	Holdup ratio	[-]
k	Turbulent kinetic energy	[kg/(m·s)]
Q	Volumetric flow rate	[m^3/s]
$R1$	Inner radius pipe	[m]
$R2$	Outer radius pipe	[m]
Re	Reynolds number	[-]
T	Temperature	[°C]
Tw	Scaled water thickness	[-]
U	Flow velocity	[m/s]
u^*	Friction velocity	[m/s]
U_s	Superficial velocity	[m/s]

1

Introduction

Heavy oil resources are becoming more important due to the decaying amount of available light oils. But these heavy oils have a practical disadvantage in the exploration process. The name heavy refers to the high viscosity property which is responsible for a high wall resistance when pumped through a pipeline. This results in large pressure losses and high operating cost.

Technologies to decrease the wall resistance of heavy oils are required. An efficient technique to achieve this is water-lubricated flow. This flow regime, where oil flows through the core of a pipeline surrounded by a lubrication film of water, is ideal for heavy oil transportation. In the multiphase flow field this flow regime is known as core-annular flow (CAF). The pressure loss in the pipeline decreases significantly which makes the operating conditions better and affordable.

The best CAF pipeline example is the pipeline of Shell in the North Midway Sunset Reservoir. This pipeline in California has been used from 1970 till 1982. Despite the high efficiency and low investment cost this technique is not used frequently. The possibility of the oil core touching the pipe wall is a main reason for the rare use of CAF. This occurrence, which is called fouling, increases the pressure loss largely with the possibility of even damaging the transportation line. A better understanding of CAF behavior is needed to improve this technology and to optimize the operating conditions.

Already a century ago (Isaacs & Speed, 1904) the study of CAF started with a high increase in research activity in the last few decades. At the University of Minnesota quite some research has been done on vertical and horizontal core-annular flow by Bai (1992), Arney (1993), Joseph et al. (1997) and Li and Renardy (1999). But also at more places around the world the CAF phenomenon has drawn the attention. For example Charles (1961) and McKibben (2000) in Canada, Bannwart (2004) at the University of Campinas in Brazil, Grassi et al. (2008) and Sotgia et al. (2008) at the University of Brescia and Modena in Italy and Al-Awadi (2011) and Alagbe (2013) at the Cranfield University in the UK. In addition to the experimental work, the state-of-the-art technique of computational fluid dynamics (CFD) has been used more frequently during the last two decades. The numerical work started with the assumption of a rigid core with imposed waves as empirical input. With the strong development of the field of CFD the results are faster and more accurate. Setting up a numerical simulation for a single phase pipe flow is well-known these days, but a two phase CAF simulation is still a field of development.

Both experimental and numerical techniques are of equal importance in the field of fluid mechanics. Both techniques have their own pros and cons. Specific experimental techniques have limited applicability ranges, can be expensive and it can be hard to access all valuable information. In numerical simulations these problems are less relevant. Parameters can easily be varied, all data are accessible and simulations are a lot cheaper. Numerical results on the other hand depend on mathematical models and calculation methods with inherent errors. For numerical results it is always important to check if the results are realistic, whereas experiments are dealing with real flows. Both techniques are widely used nowadays to validate each other and to use the benefits of both techniques.

Ooms (1972) and Oliemans (1986) studied the CAF phenomenon with experiments and theory at the Delft University of Technology and recently students started graduating on the CAF topic. This started with Beerens (2013) followed by Ingen Housz (2016), Radhakrishnan (2016) and van Duin (2017).

Beerens continued the work of Li and Renardy (1999) with numerical simulations with an improved volume of fluid method for vertical CAF. Beerens validated his work with experiments from Bai et al. (1992). Periodic boundary conditions were used in the main flow direction to reduce the simulation time. With the use of periodic boundary conditions the length of the waves on the interface is restricted. Beerens performed a good validation to support his chosen domain length and finished his work with the start of horizontal CAF simulations.

Ingen Housz continued the numerical work for horizontal core-annular flow with a slightly improved numerical solver. Ingen Housz found that a turbulence model was needed and validated his numerical results by performing experimental work in the laboratory of Process and Energy. For the experiments a minimum pressure loss was found at a water addition of 12%. In the numerical work the wall friction was underestimated which resulted in too high mixture velocities.

Radhakrishnan directly followed up the work of Ingen Housz by also performing numerical and experimental studies. Radhakrishnan investigated the temperature dependency for vertical and horizontal CAF. In the end of his work Radhakrishnan changed the set-up of the simulations. So far the simulations were driven by a prescribed pressure gradient. Radhakrishnan changed this according to Kouris and Tsampopoulous (2001) by forcing an imposed total flow rate. The advantage of this set-up is that it is more in line with the experiments.

Van Duin (2017) continued Radhakrishnan's experimental work and started with improving the set-up. An extensive investigation to the oil viscosity influence was done and different scaling parameters have been investigated. The results were compared with Ingen Housz and visualizations have been done with a high-speed camera.

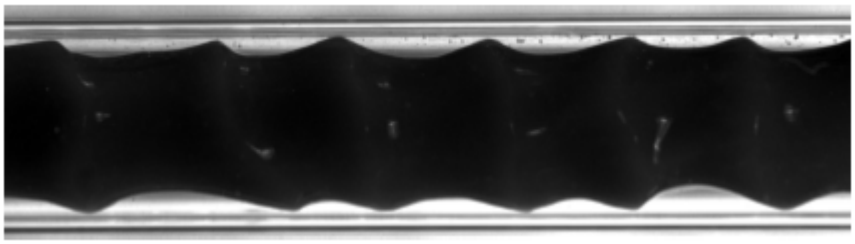

Figure 1.1: Visualization of horizontal CAF by van Duin [1].

The use of the solver with imposed flow rates, which ended the simulation study by Radhakrishnan, is the start of the present research. The experimental results of van Duin are tried to be reproduced with numerical calculations. In chapter 2 some theoretical background on multiphase flow is given, whereas chapter 3 gives some background on the experiments. In chapter 4 the numerical settings are described and in chapter 5 the first numerical results are given. In the first numerical results it is tried to reproduce the experiments with 20% water cut for different temperatures (giving different viscosities). In chapter 6 a grid dependence study is performed and two different solvers are compared. Chapter 7 describes new numerical results for different water cuts and pressure gradients at 40°C. The report is finished with holdup estimations that are derived from the flow visualization experiments (see figure 1.1) by van Duin.

2

Multiphase flows

Core-annular flow is a multiphase flow phenomenon. The two phases are both fluids and the flow can be characterized by different flow patterns and corresponding dimensionless numbers. These characteristics are described in this chapter together with the used definitions. At the end of the chapter two different theories are given about the levitation mechanism of the core and an analytical model is described.

2.1. Flow patterns

Different distributions are available for two immiscible fluids flowing through a pipe. Two-phase pipe flow can be classified according to these distributions, which usually are referred to as flow regimes or flow patterns. Which flow pattern can be expected depends on different operating conditions. The physical properties of the fluids, the pipe geometry, the flow rates, the volume ratio and the operating pressure and temperature are all of influence. For an oil-water pipe flow different flow patterns are

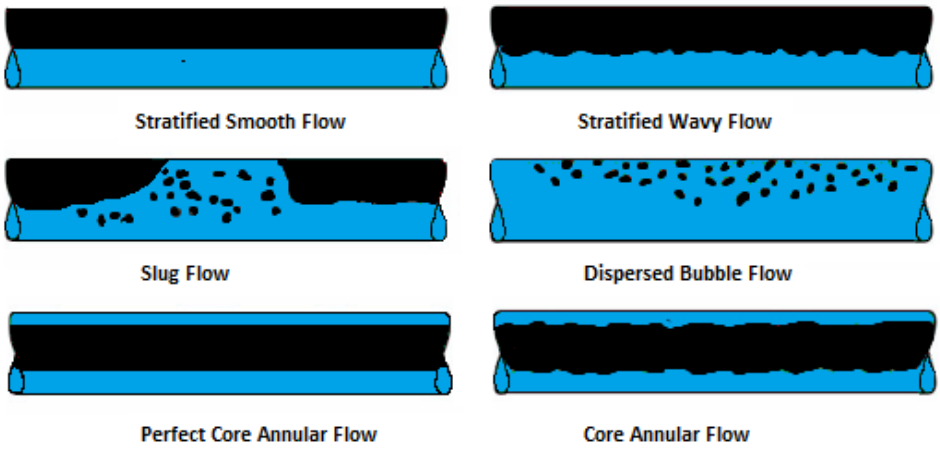

Figure 2.1: Flow patterns for oil and water flow through a horizontal pipeline. Black indicates oil and blue indicates water.

shown in figure 2.1. The oil has a lower density than water. Due to the density difference gravity will push the water to the lower part of the pipe and buoyancy will cause the oil to flow in the upper part of the pipe. For relatively low flow rates stratified smooth flow is likely to occur. When increasing the velocity difference between the two fluids instabilities at the interface can develop resulting in stratified wavy flow. Bubble flow is a flow pattern when in particular the water flow rate is higher than the oil flow rate. The oil bubbles, which actually are droplets, will settle mainly in the top of the pipe due the density difference. These droplets can differ in size but when these droplets grow sufficiently large the flow pattern will transfer into slug flow. Slug flow in pipelines is unwanted because this flow pattern

is creating high pressure fluctuations. The flow regime of interest for this research is when the oil flows through the center of the pipe with the water in an annulus around it. With the water completely surrounding the oil, the oil is not touching the pipe wall. Not only should the oil flow rate be higher than the water flow rate, all other operating conditions are also of importance to maintain this flow regime. An eccentric position of oil in the pipe can be observed due to the density difference and instabilities at the interface will likely occur due to a velocity difference. A concentric oil core with a smooth interface, known as perfect core-annular flow (PCAF), is rarely seen in practice.

Different investigations have been conducted to determine the dependence of different factors on the flow pattern. These results are often presented in a flow pattern map for which an example is given in figure 2.2. For a horizontal pipe different regimes are plotted as function of the water and oil velocities. Such a flow map is created for a specific pipe size and specific values for the other important operating conditions. The flow pattern map will differ when some conditions are changed. The boundaries between the flow regimes are denoted by lines. The transitions between different regimes are caused by growing instabilities which are hard to predict with a very good accuracy. The lines have to be seen more as transitions zones.

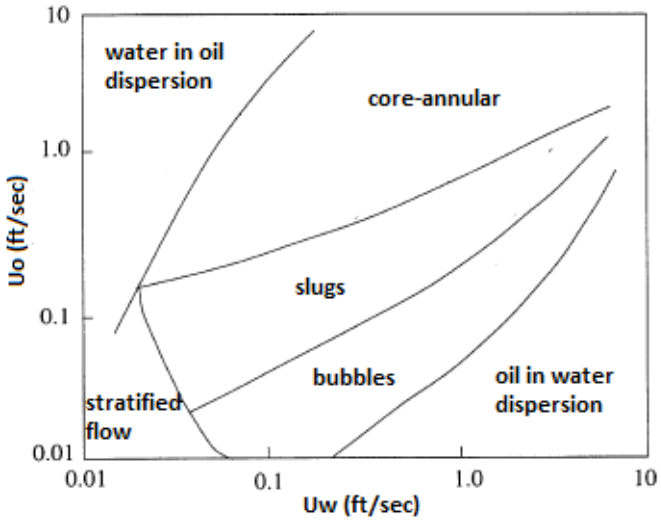

Figure 2.2: Flow map of horizontal flow when the oil is lighter than water [2].

2.2. Definitions

In this section some definitions are given which are used in the report. On the left side of figure 2.3 the front view of PCAF is sketched. For PCAF the oil is settled perfectly in the center of the pipe. On the right side core-annular flow is sketched observed in reality due to the eccentric position of the core and the waves at the interface. In the figure the areas of oil and water are specified. With the notation of U_O and U_W for the oil and water velocities respectively the following definitions are defined:

- Volumetric flow rates:

$$Q_O = U_O A_O, \qquad Q_W = U_W A_W \qquad (m^3/s) \tag{2.1}$$

- Superficial velocities:

$$u_{SO} = \frac{Q_O}{A} = \frac{U_O A_O}{A}, \qquad u_{SW} = \frac{Q_W}{A} = \frac{U_W A_W}{A} \qquad (m/s) \tag{2.2}$$

- Phase holdups:

$$H_O = \frac{A_O}{A}, \quad H_O = \frac{A_W}{A}, \quad H_O + H_W = 1 \tag{2.3}$$

- Water addition / water cut:

$$\epsilon_W = \frac{Q_W}{Q_O + Q_W} \tag{2.4}$$

- Holdup ratio:

$$h = \frac{Q_O/V_O}{Q_W/V_W} = \frac{Q_O/Q_W}{V_W/V_O} \tag{2.5}$$

The superficial velocity and holdup ratio are two common definitions for multiphase pipe flow. The superficial velocity is the velocity when each phase would flow through the pipe as a single phase flow. The holdup ratio is an important core-annular flow definition and it is the ratio between the ratio of the flow rates and the ratio of the in situ volume fractions. When the holdup ratio is smaller than unity the oil phase is accumulating and when larger then unity the water phase is accumulating. In the experiments of Bai et al. [29] the interesting result was found that the holdup ratio was approximately 1.39 for all their CAF experiments.

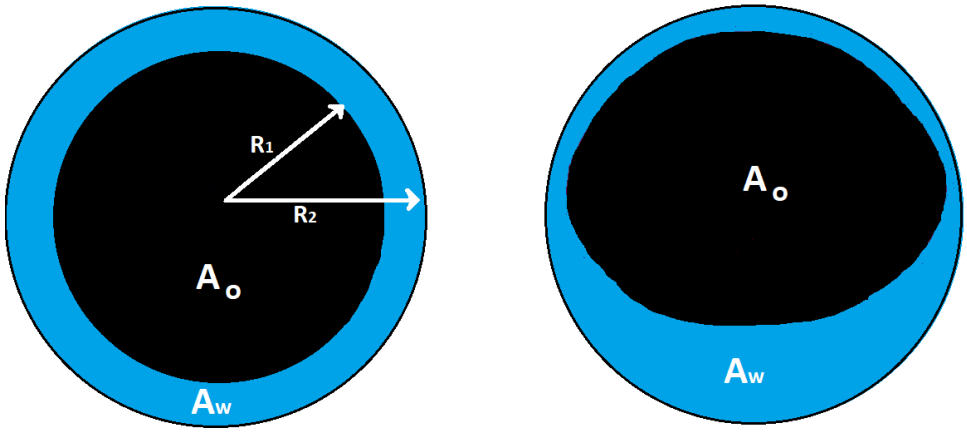

Figure 2.3: Sketch of PCAF (left) and realistic CAF (right).

For the specific case of PCAF, where the core is exactly at the center with R1 and R2 as defined in figure 2.3, the following definitions are applicable,

- Volumes PCAF:

$$V_O = \pi R_1^2 L, \quad V_W = \pi(R_2^2 - R_1^2)L \tag{2.6}$$

- Holdup ratio PCAF:

$$h = \frac{Q_O/Q_W}{V_O/V_W} = \frac{Q_O}{Q_W}\frac{\pi(R_2^2 - R_1^2)L}{\pi R_1^2 L} = \frac{Q_O}{Q_W}\left(\frac{R_2^2}{R_1^2} - 1\right) \tag{2.7}$$

2.3. Non-dimensional numbers

Results with dimensions are often difficult to interpret. Therefore nondimensionalization is a well known technique in fluid dynamics as this has several advantages. By taking the ratio of relevant forces of the problem several dimensionless numbers can be created. These dimensionless numbers give insight on the importance of the different terms which makes it easier to understand the physics. Five forces which play a role in multiphase flow with a characteristic length L and velocity U are:

- Inertial Force: $\sim \rho U^2 L^2$
- Viscous Force: $\sim \mu U L$
- Surface tension: $\sim \sigma L$
- Gravitational Force: $\sim \rho g L^3$
- Pressure Force: $\sim \Delta p L^2$

With these forces the following familiar dimensionless numbers can be created:

$$\text{Reynolds number (Re)} = \frac{\text{Inertial force}}{\text{Viscous force}} = \frac{\rho U^2 L^2}{\mu U L} = \frac{\rho U L}{\mu} \tag{2.8a}$$

$$\text{Froude number (Fr)} = \sqrt{\frac{\text{Inertial force}}{\text{Gravitational Force}}} = \sqrt{\frac{\rho U^2 L^2}{\rho g L^3}} = \sqrt{\frac{U^2}{gL}} \tag{2.8b}$$

$$\text{Eötvös number (Eö)} = \frac{\text{Gravitational force}}{\text{Surface tension}} = \frac{\rho g L^3}{\sigma L} = \frac{\rho g L^2}{\sigma} \tag{2.8c}$$

These numbers are expressed for a single phase flow and have been adjusted for two phase flow. The Reynolds numbers for the water and oil phases can be expressed in terms of their superficial velocities:

$$Re_{sw} = \frac{\rho_o U_{sw} D}{\mu_w}, \tag{2.9a}$$

$$Re_{so} = \frac{\rho_o U_{so} D}{\mu_o}. \tag{2.9b}$$

For the Froude number the buoyancy force on the core is important. Therefore the density difference is taken into account giving:

$$Fr = \sqrt{\frac{\rho_o}{\Delta\rho}\frac{U^2}{gL}}. \tag{2.10}$$

Another advantage of dimensionless numbers is the independency of the units. This independency makes it easier to compare results which are obtained for different systems. For core annular flow Li and Renardy (1999) defined the following dimensionless numbers:

$$\text{Viscosity Ratio:} \quad m = \frac{\mu_W}{\mu_O} \tag{2.11a}$$

$$\text{Density Ratio:} \quad \xi = \frac{\rho_W}{\rho_O} \tag{2.11b}$$

$$\text{Radius Ratio:} \quad a = \frac{R_2}{R_1} \tag{2.11c}$$

$$\text{Surface tension parameter:} \quad J = \frac{\sigma^\star R_1 \rho_o}{\mu_o^2} \tag{2.11d}$$

Next to these numbers two new dimensionless numbers are used in the present report. Special attention is given to the interface shape and the thickness of the water layer around the core. The radial notations from figure 2.3 are used and the notations for the crest and trough from figure 2.4 are applied. The crest and trough heights are defined from the center line of the pipe, which are used in the following quantities:

$$\text{Amplitude:} \quad A^* = \frac{Y_{crest} - Y_{trough}}{2R_1} \tag{2.12a}$$

$$\text{Water Thickness:} \quad Tw = \frac{R_2 - 0.5\left(Y_{crest} + Y_{trough}\right)}{R_2} \tag{2.12b}$$

Figure 2.4: Trough and crest of the waves at the bottom and top interface of a slice through the length of the pipe.

2.4. Levitation

Due to the density difference between oil and water there is an upward buoyancy force on the oil core pushing the core in an eccentric position. To prevent the oil from rising further upwards there has to be another force counterbalancing this upward buoyancy force. Two different theories exist in the literature in which the waves at the interface play a crucial role. Without the waves at the interface core-annular flow is not stable.

The lubricated-film model was proposed by Ooms and Oliemans [10]. In this model the inertia terms are neglected with respect to the viscous terms and the interface has a rippled shape. The movement of the interface with respect to the pipe wall creates pressure variations in the water film at the top which exerts a downward force on the oil core. An asymmetrical shape of the waves is therefore important. This asymmetry creates a higher pressure build-up before the wave crest than a pressure drop after the wave crest. This creates a pressure difference between the top and bottom which can grow so large that it counterbalances the buoyancy force on the core. The ripples on the interface must have a sharp angle before the crest and a smooth angle after the crest.

The second model is the flying-core model of Joseph et al. [2]. In this model the inertia terms are not neglected which changes the theory. They state that the ripple shapes are unstable since the pressure is high at the location where the gap is the smallest. The waves are therefore sharp where it was smooth and smooth where it was steep, resulting in the flying core model. Due to the inertia forces the build-up of pressure after the wave crest is now larger than the pressure drop before the wave crest. This creates again a force downwards which counterbalances the buoyancy force on the core.

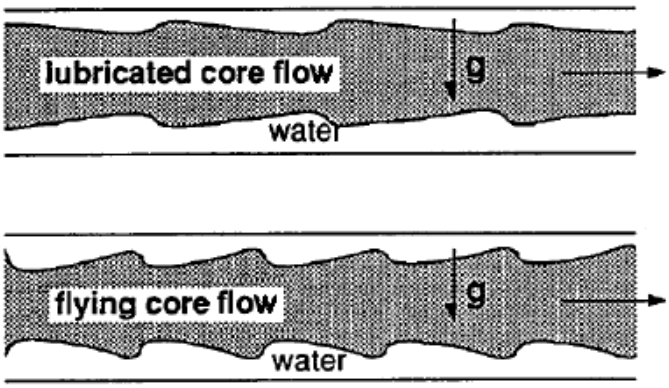

Figure 2.5: Schematic representation of the lubricated-film model and the flying-core model.[2].

2.5. Analytical model

Besides the experimental and numerical technique also the analytical model of Ullmann & Brauner [24] is used to study the core-annular flow phenomenon. This model can predict the pressure drop of core-annular flow with a laminar core and turbulent annulus. A two-fluid model is used where Ullmann & Brauner derived closure relations for the interfacial and wall shear stress. After the closure relations are applied the scaled pressure drop is predicted with,

$$\frac{dP_{CAF}}{dP_{oil}} = \frac{X^2}{H_W{}^2}. \tag{2.13}$$

In this equation is X the Martinelli parameter, which expresses the phase fraction of a flowing fluid. Ullmann & Brauner derived this parameter as:

$$X^2 = \frac{0.046}{16}\left(\frac{\mu_w}{\mu_o}\right)^{0.2}\left(\frac{\rho_w}{\rho_o}\right)^{0.8}\frac{Re_{so}{}^{0.8}}{\tilde{Q}^{1.8}}, \tag{2.14}$$

where Re_{so} is the Reynolds number based on the superficial oil velocity and $\tilde{Q}$ the ratio of the oil and water flow rates. The water holdup fraction, H_W, is derived by Ullmann & Brauner as:

$$H_W = \frac{\frac{c_i}{2} - X^2\tilde{Q}F_i^{-1} + \frac{c_i}{2}\left[1 + 4X^2\left(\frac{\tilde{Q}}{c_i}\right)^2 F_i^{-1}\right]^{0.5}}{c_i + \tilde{Q} - X^2\tilde{Q}F_i^{-1}}, \tag{2.15}$$

where c_i is the slip parameter and F_i the interfacial friction factor. The slip parameter is taken as 1.17 and the interfacial friction factor as 1, according to Ullmann & Brauner [24].

With these relations the scaled pressure drop is estimated. The dimensional pressure drop is obtained by multiplying the scaled pressure drop by the pressure drop of a single phase flow of oil at the same conditions. The oil phase is laminar as the Reynolds number of oil is not higher than 50. The pressure drop can therefore be calculated as:

$$\frac{dP_{oil}}{dZ} = \frac{128}{\pi}\frac{\mu_O Q_O}{D^4} \tag{2.16}$$

.

3

Experimental approach

Since numerical simulation use all kind of models and assumptions it is always important to validate the results. The simulations in this research are validated with van Duin's experiments. A brief description of the set-up is given in this chapter together with the used oil properties. Different temperatures are investigated during the experiments to study the effect of the viscosity on the pressure losses. For a water cut of 20% the results are given in section 3.2. For more results and for a more thorough description the work of van Duin [1] should be consulted.

3.1. Physical properties

The core-annular flow is investigated with the very viscous oil $Shell\ Morlina\ S2\ B\ 680$ and simple tap water. In the experiments the temperature effect on the flow is investigated. The density and viscosity change with the temperature, see the measurements results for the density in figure 3.1 and for the viscosity in figure 3.2. The water properties are added in the figures using data from [3] for the same temperature range.

The density and viscosity decrease with increasing temperature. The density of water drops a bit more than oil so the density ratio ξ increases a bit. This difference is however very small. The ratio between the viscosities is very large, the oil is between 1000 and 3000 times more viscous than water. The ratio of the viscosities increases with approximately a factor of 5 from 20°C to 50°C. During the experiments only the oil has been heated up and the water is injected at room temperature. In the simulations water is taken at the same temperature as the oil core. No influence is expected in the results for this difference as the viscosity of water is already very low compared to the oil viscosity.

Another physical property which plays a role in multiphase flow is the surface tension σ. Surface tension is a result of an uneven attraction of molecular forces between different phases. This creates a surface force which could be seen as an elastic skin. For liquid-liquid interfaces this phenomenon is referred to as the interfacial tension γ. The interfacial tension between water and oil has been measured by a $Krüss$ ring tensiometer at Shell Amsterdam. The interfacial tension has been measured at the start of the experiments and at the end when all the experiments were completed; see table 3.1. Due to the interaction of oil and water in the experiments the interfacial tension can change. This can influence the surface tension when the oil is reused.

Table 3.1: Measured interfacial tension at 20°C [1].

Oil Sample	Measurement
Start	$13.8 \cdot 10^{-3}$ N/m
Used	$16.9 \cdot 10^{-3}$ N/m

These measurements were somewhat unexpected as it would physically be more logical for the interfacial tension to remain constant or decrease. The unexpected trend is probably due to the susceptible technique for measurements errors. The interfacial tension is only measured at 20°C. The literature suggests that the interfacial tension is not changing much to at least 50°C but this is something that still should be validated with measurements. The surface tension measurements for the used oil were not available at the start of the simulations and are therefore chosen as $16 \cdot 10^{-3}$ N/m from the experiments of Ingen Housz. In retrospect this value can be assumed to be in the suitable range.

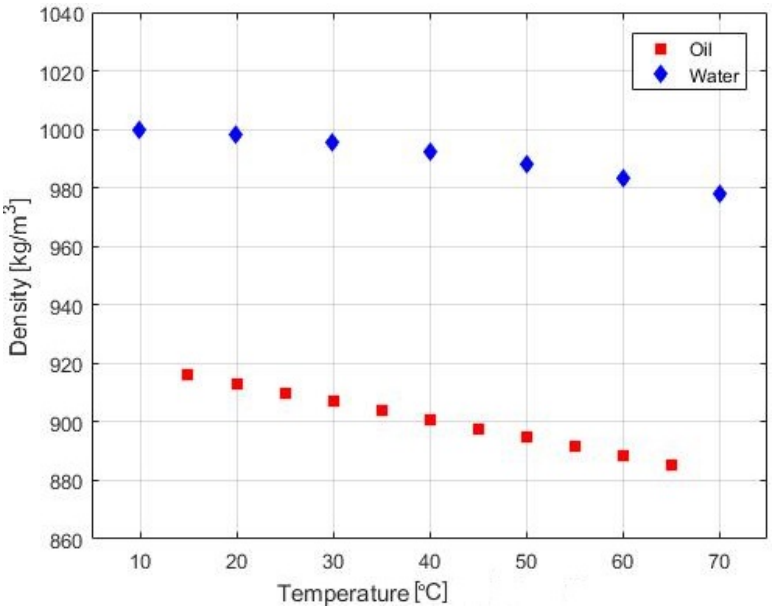

Figure 3.1: Water density [3] and measured oil density [1].

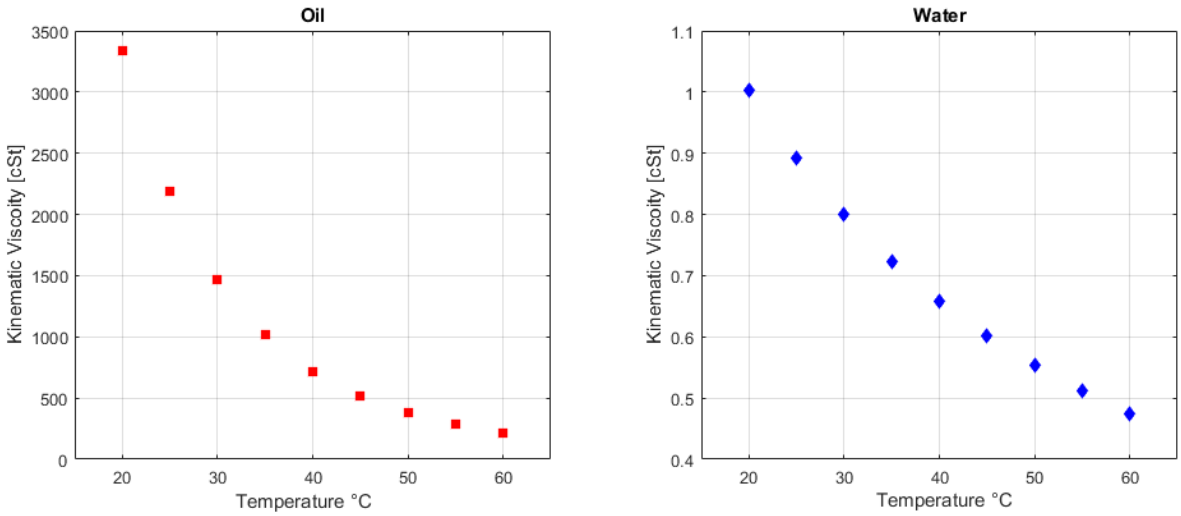

Figure 3.2: Water viscosity [3] and measured oil viscosity [1].

3.2. Experimental results

The experiments were performed at the lab of Process and Energy at the TU Delft. The used pipe was approximately 7.5 meter long with an inner diameter of 21 millimeter. The pipe is built up by a divider for creating CAF at the inlet followed by a 2 meter straight section. Thereafter a 180 degree bend is followed by a 3 meter straight section, another 180 degree bend and the last 0.25 meter straight section. In the horizontal 3 meter section the relative pressure drop is measured by two pressure probes sufficiently far away from the bends. After the last straight section the fluids are collected in a large vessel. Due to the density difference the oil and water are separated after one day. As the oil is not recirculated in the pipe, it is assumed that the temperature of the oil is not decreasing significantly during the experiments.

The oil is heated by a device in front of the inlet to the desired temperature. The oil is pumped into the pipe by a frequency driven pump to a flow rate of approximately 0.345 liter per second. The tap water flow rate is adjusted such that the water cut of interest is obtained. The water cut during the experiments has been varied from 9 to 25%. For the first numerical simulations the water cut is restricted to 20%. The experimental results are given in table 3.2.

Table 3.2: Experimental results from van Duin [1] for a water cut of 20%.

Oil flow rate $[m^3/s]$	Water flow rate $[m^3/s]$	Water cut [%]	Temperature [°C]	Oil viscosity [cSt]	Pressure drop [Pa/m]
$0.3450 \cdot 10^{-3}$	$8.638 \cdot 10^{-5}$	20.02	21.28	3338	1004
$0.3450 \cdot 10^{-3}$	$8.635 \cdot 10^{-5}$	20.02	30.92	1472	1086
$0.3449 \cdot 10^{-3}$	$8.628 \cdot 10^{-5}$	20.01	38.91	718	1123
$0.3448 \cdot 10^{-3}$	$8.637 \cdot 10^{-5}$	20.03	48.21	383	1045

4

Numerical method

Computational Fluid Dynamics (CFD) is the study of predicting fluid flow using numerical calculations. Numerical calculations are done because analytical solutions are only possible for simple mathematical equations. Hence, CFD is an area of interest that over the last decades has increased in popularity due to the increase in computer power. CFD has transformed from a more mathematical curiosity into an essential tool used in almost all branches of fluid mechanics.

For simulating horizontal core-annular flow the open source CFD package OpenFOAM is used for setting up the calculations. The geometry and mesh are created with the software GAMBIT. In this chapter the solution method is described with all the used models.

4.1. Problem formulation

The start of simulating a physical problem with CFD is setting up a mathematical description of the physical phenomena. The physical laws are translated with mathematical relations into partial differential equations. For a correct modeling the relations have to be chosen carefully but, as will be explained, sometimes assumptions need to be made for simulating the physical problem.

4.1.1. Navier Stokes equations

The Navier-Stokes equations are the basic governing equations for a viscous fluid. They consist of two parts: the conservation equations for mass and the conservation equations for momentum. The mass conservation equation is also referred to as the continuity equation. The momentum equations are derived from applying Newton's second law to a fluid element. The final form contains an inertia, pressure and viscous term. For a three dimensional problem the momentum equation consist of three equations, one for each direction.

$$\frac{\partial \rho}{\partial t} + \nabla \cdot (\rho \vec{u}) = 0, \qquad \text{Continuity equation.} \tag{4.1}$$

$$\rho \frac{D\vec{u}}{Dt} = -\nabla p + \nabla \vec{\tau} + \rho \vec{g}, \qquad \text{Momentum conservation equation.} \tag{4.2}$$

Equation 4.2 uses the material derivative which is defined as:

$$\frac{D\vec{u}}{Dt} = \frac{\partial \vec{u}}{\partial t} + \vec{u} \cdot \nabla \vec{u}. \tag{4.3}$$

The material derivative describes the velocity change of a fluid particle while moving with the fluid flow. The viscous term is linearly proportional to the velocity derivative of the fluid when the fluid is Newtonian.

$$\nabla \vec{\tau} = 2\mu \Delta \vec{S}, \tag{4.4}$$

$$\vec{S} = \frac{1}{2}\left(\nabla \vec{u} + \nabla \vec{u}^{T}\right). \tag{4.5}$$

For an incompressible fluid the assumption is made that the density is constant. Therefore the density can be taken outside the spatial derivative and the time derivative is equal zero, $\partial\rho/\partial t = 0$. This results in the Navier Stokes equation for an incompressible, Newtonian fluid:

$$\nabla \cdot \vec{u} = 0 \tag{4.6}$$

$$\rho \frac{D\vec{u}}{Dt} = -\nabla p + \mu \Delta \vec{u} + \rho \vec{g}. \tag{4.7}$$

4.1.2. Volume of Fluid Method

Equations 4.6 and 4.7 are the Navier Stokes equations for a single phase flow. Because core-annular flow is a two phase flow the equations need some adjustments. Different approaches to solve such two phase problem are available. In this research the 'Volume of Fluid' (VOF) method is used. In the VOF method both fluids are treated as a single homogeneous fluid where an indicator function α is used which represents the fluid fraction. The indicator function is restricted to $0 \leq \alpha \leq 1$ where a value of zero refers to the water phase and a value of one to the oil phase. As the phases move through the flow domain the indicator function is tracked with an additional equation:

$$\frac{\partial \alpha}{\partial t} + \nabla \cdot (\vec{u}\alpha) = 0. \tag{4.8}$$

This indicator equation is a continuous function; therefore α varies over some space near the interface form zero to one. In reality the oil and water are immiscible which means that they should be modeled with a discontinuous function with only values of zero and one. The indicator function should be as less diffusive as possible to simulate the reality as good as possible. The VOF method of OpenFOAM takes care of this by making use of the MULES solver for the second term of 4.8. The MULES solver uses two different schemes for this advection term. A straightforward upwind scheme away from the interface and a more sophisticated treatment close at the interface. The more sophisticated treatment is a higher order method with an interfacial compression flux to reduce the numerical diffusion. A fine grid is however still needed at the interface for a correct modeling. With the indicator function the viscosity and density in the momentum equations are replaced by a weighted average.

$$\rho = \alpha\rho_{\text{oil}} + (1-\alpha)\rho_{\text{water}} \tag{4.9}$$

$$\mu = \alpha\mu_{\text{oil}} + (1-\alpha)\mu_{\text{water}} \tag{4.10}$$

As a last adjustment for two phase flow the interfacial tension is taken into account. This is done by adding a surface force $f_i^\star$ to the momentum equations. The surface force is modeled according to Brackbill et al. [17] with κ being the curvature of the interface surface.

$$\vec{f^\star} = -\sigma^\star \kappa \nabla \alpha \tag{4.11}$$

$$\kappa = -\nabla \cdot \vec{n} \tag{4.12}$$

The surface force is modeled as a volume force which simulates the surface pressure on the interface. The discontinuous tension is replaced by a smooth function over a small transition region along the interface with a length comparable to the computational mesh.

4.1.3. Turbulence

In the report of Ingen Housz it was found that the oil core is laminar but that turbulence can be present in the water annulus. An appropriate treatment of the turbulence will therefore be important to obtain good results. Turbulence can be expected when the inertia forces are much larger than the viscous forces. This corresponds to a sufficient high Reynolds number (2.9b). As the Reynolds number is inversely proportional with viscosity, the Reynolds number of oil is much lower than that of water. This explains the occurrence of turbulence only in the water annulus. The governing equations obtained in section 4.1.1 and 4.1.2 have to be adjusted to incorporate turbulence into the model.

Turbulence modeling

Turbulence is a property of the flow which can be featured by chaotic changes in pressure and velocity. To model the chaotic fluctuations a very fine grid is required which results in very high computational cost. Using the Reynolds averaged Navier-Stokes (RANS) equations reduces the computational cost by solving only the statistically averaged quantities which allows for using a coarser grid. For obtaining the RANS equations the fluctuating pressure and velocities quantities are first separated with a Reynolds decomposition. The pressure and velocity are separated into a time-average and the perturbations around them,

$$p = P + p' \tag{4.13}$$

$$\vec{u} = \vec{U} + \vec{u}'. \tag{4.14}$$

The capital letters refer to the time-average quantities and the accent marks to the perturbations. These decompositions are inserted into the Navier-Stokes equations and then averaged to obtain the equations for the averaged motion. With this final averaging all fluctuating parts are cancelled out except the part in the non-linear advection term. This part will result in an extra term $-\rho\overline{u_i' u_j'}$ which can be rewritten as the Reynolds stress τ_{ij}^{turb} for the incompressible RANS equations:

$$\nabla \cdot \vec{U} = 0, \tag{4.15}$$

$$\rho \frac{D\vec{U}}{Dt} = -\nabla P + \nabla(\vec{\tau}^{\text{visc}} - \vec{\tau}^{\text{turb}}) + \rho\vec{g}. \tag{4.16}$$

The Reynolds stress is a new term which has to be modeled to close the equations. This is known as the closure problem in turbulence. A way to start closing the RANS equations is to use the Boussinesq hypothesis. This hypothesis models the Reynolds stress with a linear constitutive relationship. It introduces a new concept of the eddy viscosity μ_t and turbulent kinetic energy k.

$$\vec{\tau}^{\text{turb}} = \mu_t \left(\nabla\vec{U} + \nabla\vec{U}^T\right) - \frac{2}{3}\rho k\bar{\delta}, \tag{4.17}$$

where $\bar{\delta}$ is the Dirac delta function. This hypothesis uses the idea of modeling the Reynolds stress with an eddy viscosity μ_t in the same way as the viscous stress for a Newtonian fluid is modelled with the molecular viscosity μ. This assumption is not generally valid and it is a great simplification.

Low Reynolds k-ϵ model of Launder Sharma

With the Boussinesq hypothesis the RANS equations can be closed with different closure models. The $k-\epsilon$ model is one of the most common models used in CFD for turbulence. It is a two equation model which gives a general description of turbulence by means of two transport equations. The first equation is for the turbulent kinetic energy and the second for the turbulent dissipation ϵ. As the core-annular flow experiments can be classified with a low Reynolds number the specific low Reynolds $k-\epsilon$ model of OpenFOAM is used. This model has additional damping functions and extra source terms close to solid walls.

$$\mu_t = C_\mu f_\mu \rho \frac{k^2}{\epsilon} \tag{4.18a}$$

$$\frac{\partial k}{\partial t} + \frac{\partial}{\partial x_j}\left(kU_j - \left[\mu + \frac{\mu_t}{\sigma_k}\right]\frac{\partial k}{\partial x_j}\right) = \frac{\tau_{ij}^{\text{turb}}}{\rho}\frac{\partial U_i}{\partial x_j} - \epsilon - D \tag{4.18b}$$

$$\frac{\partial \epsilon}{\partial t} + \frac{\partial}{\partial x_j}\left(\epsilon U_j - \left[\mu + \frac{\mu_t}{\sigma_\epsilon}\right]\frac{\partial \epsilon}{\partial x_j}\right) = \left(C_{\epsilon 1} f_1 \frac{\tau_{ij}^{\text{turb}}}{\rho}\frac{\partial U_i}{\partial x_j} - C_{\epsilon 2} f_2 \rho\epsilon\right)\frac{\epsilon}{k} + E \tag{4.18c}$$

In these equations C_μ $C_{\epsilon 1}$ $C_{\epsilon 2}$ σ_k σ_ϵ are model constants, f_1, f_2, f_μ damping functions and D, E the source terms active at the solid walls. For choosing the values of these variables the Launder-Sharma constants are chosen.

Table 4.1: k-ϵ model constants.

Model constants	Launder-Sharma
C_μ	0.09
σ_k	1
σ_ϵ	1.3
D	$2\nu\left(\frac{\partial\sqrt{k}}{\partial y}\right)^2$
E	$2\nu\nu_t\left(\frac{\partial^2 u}{\partial y^2}\right)^2$
ϵ_{wall}	0
$C_{\epsilon 1}$	1.44
$C_{\epsilon 2}$	1.92
f_μ	$e^{\frac{-3.4}{(1+R_t/50)^2}}$
f_1	1
f_2	$1-0.3e^{(\frac{-k^2}{\mu\epsilon})^2}$

Near wall treatment

Special care has to be taken for wall-bounded turbulent flow. In turbulent flow the gradients at the wall can be much higher whereby linear interpolation can give wrong results. Two different techniques are to fully resolve the boundary layers or to use wall functions. To fully resolve the boundary layers the first control volume at the wall should have an y^+ value of approximately 1. The y^+ value is a dimensionless wall distance number defined by:

$$y^+ = \frac{u^\star y}{\nu} \tag{4.19}$$

Where y is the distance to the wall, ν the kinematic viscosity of the fluid and $u_\star$ the friction velocity. The y^+ has the same form of the Reynolds number only now based on the friction velocity,

$$u^\star = \sqrt{\frac{\tau_w}{\rho}} \tag{4.20}$$

with τ_w the wall shear stress. When using wall functions the size of the first cell should be increased so that the y^+ is at least above 20. During this report the boundary layers are fully resolved in accordance with the previous simulations of Housz and Radhakrishnan.

4.2. Discretisation

As the obtained mathematical equations cannot be solved analytically they have to be solved numerically. First the partial differential equations have to be approximated with a set of linear algebraic equations for a number of discrete locations. These discrete locations are defined by a grid which is a division of the flow domain in a finite number of control volumes. Accurate results will only be obtained when enough control volumes are used. Therefore the grid should be sufficiently fine for accurate results. The grid should however not be too fine as more control volumes will results in larger computational effort. An extensive study of the grid is done in chapter 6 and until that point the domain of Radhakrishnan [6] is used. That mesh consists of 80 control volumes around the circumference of the pipe, with a length of 0.426 millimeter in the flow direction and 0.0375 millimeter in the radial direction.

The numerical discretization is carried out with the Finite Volume Method (FVM). This is a numerical technique which uses an integral form to discretize the mathematical equations of 4.1. For some terms the fluxes at the boundaries of the control volumes are needed. These fluxes are based on interpolation of the values at the center of the volumes. As the flux leaving a control volume is equal to the flux of the receiving neighbouring control volume the FVM method is conservative. This conservative property and the applicability to unstructured grids makes the FVM the mostly used numerical technique for CFD applications.

A variety of schemes can be chosen in OpenFOAM for interpolation and discretization. The selected formulas for the CAF simulations are listed in table 4.2. Also the chosen scheme for time discretization and the surface normal gradient scheme are given. The scheme for the surface normal gradient scheme allows for a non-orthogonal correction of the normal gradients at a boundary. When Gaussian integration is used also an interpolation scheme is specified.

Table 4.2: Selected numerical schemes. Term phi is used for the velocity flux, $\phi = \rho\vec{u}$.

Equation term	**Discretisation scheme**
Interpolation schemes	Linear
Surface normal gradient scheme	Corrected
Gradient schemes	Gauss linear
Laplacian schemes	Gauss linear corrected
Divergence schemes	
div(rho phi U)	Gauss limitedLinearV 1
div(phi alpha)	Gauss vanLeer
div(phirbr alpha)	Gauss interfaceCompression
div(phi epsilon)	Gauss upwind
div(phi k)	Gauss upwind
div(muEff*dev(T(grad(U))))	Gauss linear
Time scheme	Backward Euler

4.3. Time step restriction

To keep the simulation numerically stable, the time step is limited to a maximum value. The time steps is calculated in OpenFOAM by selecting a maximum value for the Courant number which is defined as,

$$\mathrm{Co} = \frac{U\Delta t}{\Delta x}. \tag{4.21}$$

By selecting a maximum value for the Courant number the maximum allowed Δt is calculated every iteration so that 4.21 is satisfied for every control volume. By selecting a maximum Courant number of one, the time steps are restricted such that a fluid element is not moving more than one length of a control volume. Also other physical timescales, which play a crucial role for stable and accurate simulations, have to be set by the Courant number. Therefore, for the core-annular simulations another Courant number is specified for only the interface,

$$\mathrm{Co}_\alpha = \frac{U_\alpha \Delta t}{\Delta x}. \tag{4.22}$$

The interface Courant number is based on only the normal velocities on the interface. Because of the large viscosity difference between water and oil the diffusivity around the interface is very large. Radhakrishnan found that the interface Courant number should be smaller than 0.01 for stable and accurate results [6]. For larger values the interface changed too much during one time iteration which led to wrong results.

4.4. Linear solvers

The finite volume discretization for partial differential equations will generate large sparse matrices. As the CFD program will spend a lot of computational time in solving these linearized equations it is an important aspect of the program to use an efficient solver. The solvers for those equations are sorted in two different categories: direct methods and iterative methods. As direct methods are more efficient for small problems are the iterative methods usually the best choice for CFD. Iterative methods scale much better with larger mesh sizes.

For iterative methods many different options are available. The different options can be divided into simple methods, incomplete factorization schemes, gradient methods and multigrid methods. The multigrid method is used for the pressure term and the gradient schemes for the other terms shown in table 4.3. The incomplete factorization schemes are used as preconditioner and smoother. For a detailed explaining about the solvers the book of Ferizger [13] or Moukalled [14] can be consulted. For all available choices the user guide of OpenFOAM can be viewed.

Table 4.3: Selected linear solver settings.

Variable	Solver	Preconditioner	Smoother	Tolerance
pcorr	PCG	DIC	-	1e-10
p-rgh	GAMG	DIC	DICGaussSeidel	1e-6
U	PBiCG	DILU	-	1e-6
epsilon	PBiCG	DILU	-	1e-8
k	PBiCG	DILU	-	1e-8

4.5. Boundary and initial conditions

Before the matrices can be solved special care has to be taken for setting the values for the control volumes at the boundary. Appropriate boundary conditions must be chosen, and also smart starting conditions must be set from where the linear solvers start the iteration process.

4.5.1. Boundary conditions

The diameter of the pipe is taken equal to 21 millimeter, which is equal to the size of the pipe used in the experiment, but the length of the pipe in the simulation is different from what is used in the experiment. Solving the full length of the pipe as used in the experiment would take a large amount of CPU time which is not feasible. To reduce the CPU time a small length of the pipe is taken and periodic boundary conditions are applied at the inlet and outlet. The periodic boundary conditions have a consequence that the wavelengths at the interface are restricted to the chosen domain length. The waves leaving the outlet are entering directly at the inlet so only an integer number of waves can occur in the domain. The length of the domain has to be chosen in such a way that it fits the physical expected wavelengths. As the physical expected wavelengths are not known these have to be estimated. Linear stability theory can for example be used, but also this is only a rough estimate. The length of the pipe for this research is taken as 25.58 millimeter, which is similar to Radhakrishnan's work [6].

Next to the periodic boundary conditions the boundary conditions at the wall need to be defined. The velocity at the wall is set to zero. The kinetic energy k is set to $1{\cdot}10^{-15}$ m^2/s^2 and and turbulent dissipation ϵ is set to $1{\cdot}10^{-15}$ m^2/s^3 as suggested in Wilcox [15].

4.5.2. Initial conditions

Analytic results for the velocities of perfect core-annular flow are derived in Li and Renardy (1998) for the core and the annulus. These velocities are taken as initial guess for the simulation with the aim that these velocities converge faster to the velocity field of CAF than an uniform velocity field.

$$\text{Core:} \qquad U(r) = 1 - \frac{mr^2}{A} \tag{4.23}$$

$$\text{Annulus:} \qquad U(r) = \frac{a^2 - r^2}{A} \tag{4.24}$$

These are the velocity profiles for horizontal CAF with the dimensionless numbers of 2.11a and 2.11c. The initial values for α are obtained by rewriting the holdup radio 2.7 into:

$$R_1 = \frac{R_2}{\sqrt{(Q_W/Q_O)h + 1}} \tag{4.25}$$

With this formula the volume of oil is determined by using the finding of Bai et al. (1992) that the holdup ratio is always 1.39. For increasing the convergence speed a small perturbation is given to the initial PCAF distribution. With this small perturbation the waves at the interface develop much faster which results in some time gain. Note that while in the experiments the volume ratio could vary due to accumulation, this is not possible in the simulations because of the periodic boundary conditions. After initializing the volumes the volume ratio is fixed for the whole simulation. The kinetic energy k is initialized with 0.2 m^2/s^2 and the turbulent dissipation with 200 m^2/s^3 to expedite the development of turbulence.

4.6. Pressure-velocity coupling

The final governing equations consist of one continuity and three momentum equations. In these four equations there are also four quantities which have to be solved: one pressure and three velocity components. The number of equations and quantities are matched but in the continuity equation the pressure component is missing. This requires a careful choice of an iterative solution procedure.

OpenFOAM has three different choices for the coupling problem. The SIMPLE algorithm, which is a technique invented by Patankar and Spalding (1972), is a predictor - corrector procedure. Based on the discretized momentum equation an initial guess for the pressure $p^\star$ is taken to calculate an intermediate velocity field $\vec{u}^\star$. The momentum equations are then satisfied but the mass fluxes at the cell faces do not have to satisfy the continuity equation. A correction to the pressure and velocity is applied with variables p' and $\vec{u}'$ so that the continuity equation is satisfied. With the guessed variables at the start and the requirement that the continuity equation has to be satisfied the corrections can be calculated and be added to the guessed values. These new pressure $p = p^\star + p'$ and velocity $\vec{u} = \vec{u}^\star + \vec{u}'$ values do satisfy the continuity equation but not the momentum equations. This procedure is repeated until convergence has been achieved.

The corrected velocities always satisfy the continuity equation. Large differences between guessed and corrected pressure values can however lead to a slow convergence or even a blow up. An under-relaxation θ can be used for the pressure correction, $p = p^\star + \theta p'$, to reach the converged state faster or to make the algorithm more stable. The values of θ are restricted between zero and one. Note that only the pressure can be under-relaxed and not the velocity terms because otherwise the continuity equation will be violated.

An algorithm to solve the coupled pressure-velocity equations for a transient problem is the PISO algorithm. It works almost the same as the SIMPLE algorithm but additional pressure-corrector stages are used. As the PISO algorithm is a transient algorithm it has a natural time limiter,

$$Co = \frac{U\Delta t}{\Delta x} \leq 1 \tag{4.26}$$

This restriction can lead to expensive computations when solving transient problems. Therefore OpenFOAM has another PIMPLE algorithm, which is a merged PISO-SIMPLE algorithm. It is a transient solver but makes use of the advantage of SIMPLE method to use under-relaxation. This method can reduce the computational cost as this removes the time limit restriction. A larger time-step can be used as Co can be larger than unity. Although the Co number is restricted to 0.01 for the simulations the PIMPLE algorithm is however still used. The PIMPLE algorithm seems to work better than the PISO algorithm because of some still unknown reasons.

4.7. Application solver

For solving an incompressible, isothermal two phase flow with immiscible fluids the application solver interFoam of OpenFOAM is used. This solver uses the finite volume method for discretisation and the volume of fluid method to track the phase fraction. With the choice of periodic boundary conditions at the inlet and outlet this has created the problem that there is no driving force. To overcome this problem adjustments have been made to this solver. The constant pressure solver has been used by Beerens, Ingen Housz and partly also by Radhakrishnan. In addition, another solver was used by Radhakrishnan which is the flux imposed solver.

4.7.1. Constant Pressure Solver

In the constant pressure solver a stream wise pressure gradient is imposed. Prescribing a pressure difference between the inlet and outlet is very common in CFD but with the periodic boundary conditions this is not possible. To overcome this, the pressure difference is imposed by adding a body force term f_p to the momentum equations. With this extra term the flow is still driven through the pipe.

$$\rho \frac{D\vec{u}}{Dt} = -\nabla p + \mu \Delta \vec{u} + \rho \vec{g} + \vec{f^{\star}} + f_p. \tag{4.27}$$

4.7.2. Flux Imposed Solver

In the flux imposed solver the total flow rate is imposed. The advantage of this solver is that it is more in line with how the experiments were performed. The pressure drop is now the result of the simulations, which is similar with the experiments. Although there is still a difference: in the experiments the individual flow rates of oil and water are imposed and not the total flow rate. This means that the flux imposed solver gives the desired total flow rate, but not the desired water cut. In fact the holdup fraction is also imposed in the simulations, whereas this is a result in the experiments. To summarize: the total flow rate and holdup are imposed in the simulations which lead to a pressure drop and water cut, whereas in the experiments the total flow rate and the water cut are imposed, which lead to a pressure drop and hold-up.

The desired total flow rate Q_{desired} is imposed and during every time step iteration the realized flow rate is calculated.

$$Q_{\text{realized}} = \int U dA \tag{4.28}$$

As there is no driving force the desired and realized total flow rate may differ. The flow velocity must be increased to get the realized and desired flow rate equal.

$$Q_{\text{desired}} = \int (U + dU) dA = \int U dA + \int dU dA \tag{4.29}$$

If dU is taken the same for all volumes, $\int dU dA = dUA$, then these equations can be rewritten into:

$$dU = \frac{Q_{\text{desired}} - Q_{\text{realized}}}{A}. \tag{4.30}$$

This incremental velocity is translated into f_f, which is a body force term defined as an acceleration term multiplied with the density. The term then has the same form as the initial term which is already in the momentum equations.

$$f_f = \frac{dU}{dt} * \frac{\int \rho dA}{\int dA} \tag{4.31}$$

The density is taken as a constant value which is a weighted average of the oil and water densities. Otherwise it is unclear for the interfoam solver which density should be used. The term f_f is added as extra body force term to the momentum equation. This force f_f can be seen as the force term which drives the flow every time to the desired flow rate. The velocity adjustment is built-in the PIMPLE algorithm so is corrected within every PIMPLE iteration.

$$\rho \frac{D\vec{u}}{Dt} = -\nabla p + \mu \Delta \vec{u} + \rho \vec{g} + \vec{f^{\star}} + f_f. \tag{4.32}$$

4.8. Decomposition

Parallel computing in CFD is used to speed up the simulation time. This improvement is achieved by executing the simulations with more processors. OpenFOAM divides the domain into smaller parts where the calculations of every part are run simultaneously on the different processors. More calculations can be run simultaneously by using more processors. In an ideal case the simulation is twice as fast when

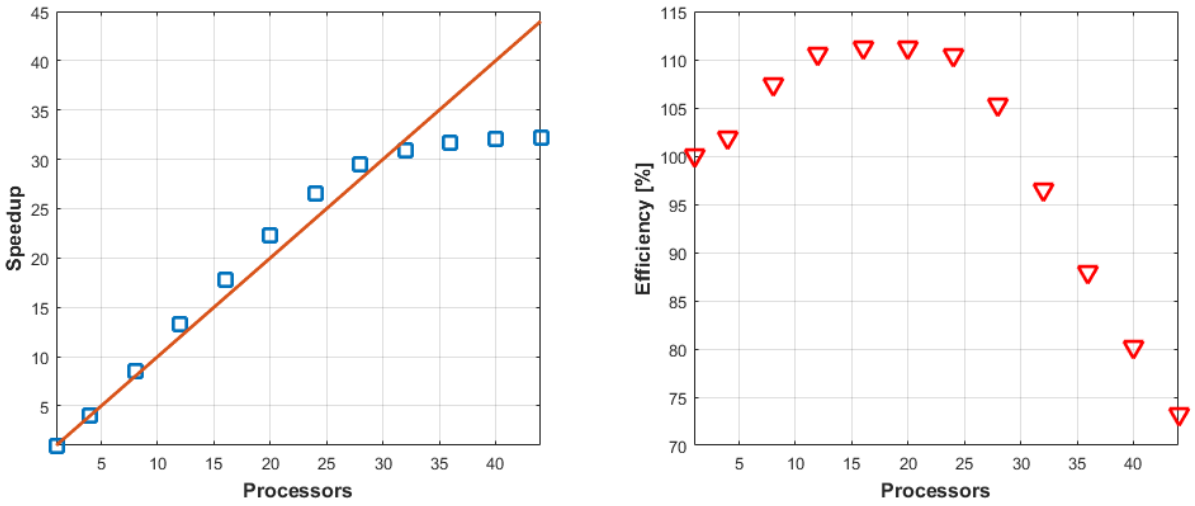

Figure 4.1: Speedup and efficiency function. Squares and triangles are the measured data.

twice the number of processors are used. In reality however there is a maximum number of processors above which no further speed up is obtained. Since the solving procedure is shared among different processors some data have to be exchanged now and then. At a certain number of processors this can slow down the simulation more than it speeds up the simulation. To run the simulations as efficient as possible this sensitivity is tested.

In figure 4.1 two graphs are shown. In the left graph the speedup is plotted against the number of used processors. The speedup is hereby defined by:

$$\text{Speedup(X)} = \frac{\text{clock time on 1 processor}}{\text{clock time on X processors}}. \tag{4.33}$$

The orange line is the linear speedup case for the ideal decomposition. It is found that with up to 30 processors the problem is scaled better than the ideal case. This occurrence is seen more often with coupled nonlinear equations. This is caused by a better use of the memory compared to the use of 1 processor. With more than 30 processors the speedup is increased a bit until 35 processors are applied, above which the speed-up can assumed to be constant. The right graph shows the efficiency as function of the number of processors. The used definition for the efficiency is:

$$\text{Efficiency(X)} = \frac{\text{Speedup(X)}}{\text{number of processors}}. \tag{4.34}$$

Until 30 processors the problem scales better than the ideal case which results in an efficiency larger than 100%. Between approximately 15 and 20 processors the efficiency is found to be at the maximum value of 111%. After increasing the number of processor above 25 the efficiency decreases rapidly. Based on these test results the simulation will be done with 24 processors. In total 28 processors are available on 1 node so with this choice there are still 4 processors free. This gives the opportunity for other users of the cluster to use the same node for smaller calculations. Note that the 24 processors have to be located at the same node to obtain the efficiency of 111%.

5

Numerical results for 20% water cut

In this chapter simulation results are compared with the experiments from table 3.2 that have a water cut of 20%. The density, viscosity and surface tension values as given in section 3.1 are used. The initialization is done according to section 4.5.2 with a holdup ratio of 1.39. The flux imposed solver is used and for all simulations the total flow rate is $0.430 \cdot 10^{-3}$ m^3/s.

Table 5.1: Parameters for the simulations I to IV.

Simulation			**I**	**II**	**III**	**IV**
Temperature		[°C]	20	30	40	50
ν_O		[cSt]	3338	1472	718	383
ν_W		[cSt]	1.00	0.80	0.66	0.55
ρ_O		[kg/m^3]	912	906	902	896
ρ_W		[kg/m^3]	998	996	993	989
R_2	$\cdot 10^{-3}$	[m]	10.5	10.5	10.5	10.5
R_1	$\cdot 10^{-3}$	[m]	9.05	9.05	9.05	9.05
σ	$\cdot 10^{-3}$	[N/m]	16.0	16.0	16.0	16.0
Q_{total}	$\cdot 10^{-3}$	[m^3/s]	0.430	0.430	0.430	0.430

The simulations were run on the cluster of 3mE of the TU Delft. A single simulation solved around 0.3 to 0.35 seconds physical time in 1 day. As the system used a slurm queuing system this resulted in 40 to 60 days of simulation time including queuing time.

5.1. Simulation I: temperature 20°C (ν_O = 3338 cSt)

Two snapshots of the water and oil distribution are presented in figure 5.1. The core-annular flow is started from a PCAF distribution. After 9 seconds, when the flow is settled, the irregular wavy interface is visible. From the slices through the three dimensional pipe there are two waves visible on the top interface and two waves at the bottom interface. On a few snapshots only one wave is visible at the bottom interface. In the longitudinal cross section the eccentricity of the oil core is also visible, which is caused by the density difference. The water layer at the top is smaller than the water layer at the bottom.

Figure 5.2 shows the ratio of the turbulent eddy viscosity and the molecular viscosity. This ratio gives an indication about how strong the Reynolds stresses are compared with the molecular stresses. Therefore it can be seen as an indication of the turbulence strength. The molecular viscosity of water is used because only turbulence in the water layer is expected. After convergence the Reynolds numbers, based on the superficial velocities, are 7 and 5390 for the oil and water flows, respectively. From the figures it is seen that this viscosity ratio only indicates some turbulence at the bottom and the maximum of the turbulence ratio is about 19. For comparison a simulation is performed where

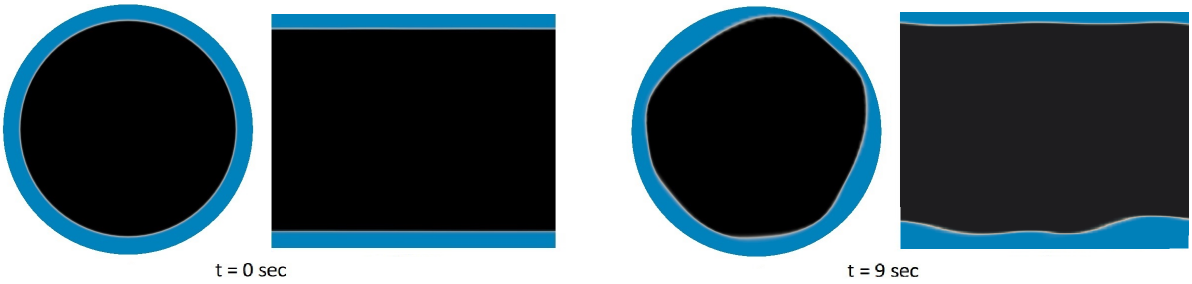

Figure 5.1: Cross-sectional snapshots of the distribution of water (blue) and oil (black) at 20°C

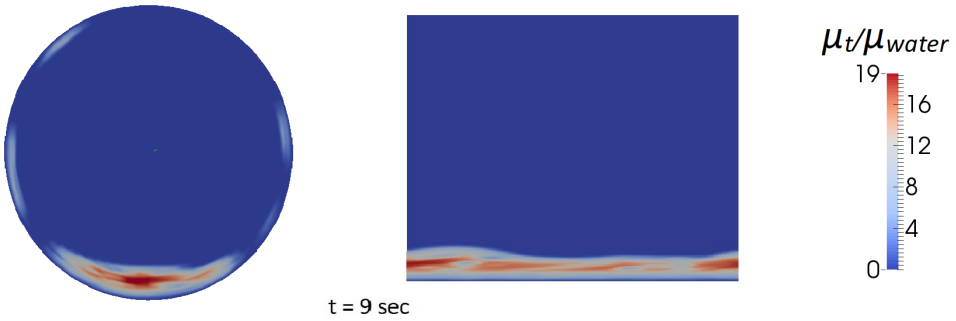

Figure 5.2: Ratio of turbulent eddy viscosity to the molecular viscosity at 20°C.

water is flowing as a single phase flow through the pipe. For the same conditions the maximum of the turbulent to molecular viscosity is found to be around 95; see figure 5.3. A ratio of 100 indicates that the flow is certainly turbulent. For the core-annular flow simulation the turbulence is somewhat reduced and only present in the water layer at the bottom.

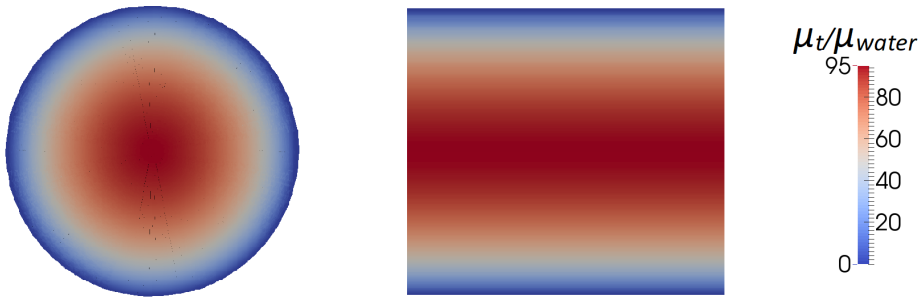

Figure 5.3: Turbulent to molecular viscosity ratio of single phase water flow.

The key results of the flux imposed solver and prescribed holdup are the water cut and the pressure gradient. For this temperature also the individual flow rates are studied more thoroughly. The flow rates are taken at the right periodic boundary face and plotted over time in figure 5.4. There are some large and small scale fluctuations visible in the graph. The flow rates are taken with a sampling time of 0.005 seconds so the small scale fluctuations are hard to see in a 9 second plot. Hence, in figure 5.5 there is a zoom in of the oil flow rate for half a second. In this figure the continuously ascending and descending behaviour at the small scale are well visible. As the flow rates are obtained from a cross section, this results in variations of the flow rates as wave crests and troughs are passing by. As the waves are randomly formed over the surface the crests and troughs at the bottom and top interface do not necessary pass by at the same time. Furthermore, the waves at the bottom interface are larger than at the top interface so these waves create larger fluctuations.

The large scale variations are linked to the different wave shapes. The numerical simulation does not converge to one specific wave size. For figure 5.5 a wave at 9.2 seconds starts growing in amplitude until around 9.4 seconds. From here, the wave amplitude starts to decrease again until shortly

after 9.5 seconds. The wave at 9.2 seconds is thereby smaller than the wave at 9.5 seconds. Note that as the waves at the upper interface are smaller they have less influence on the fluctuations.

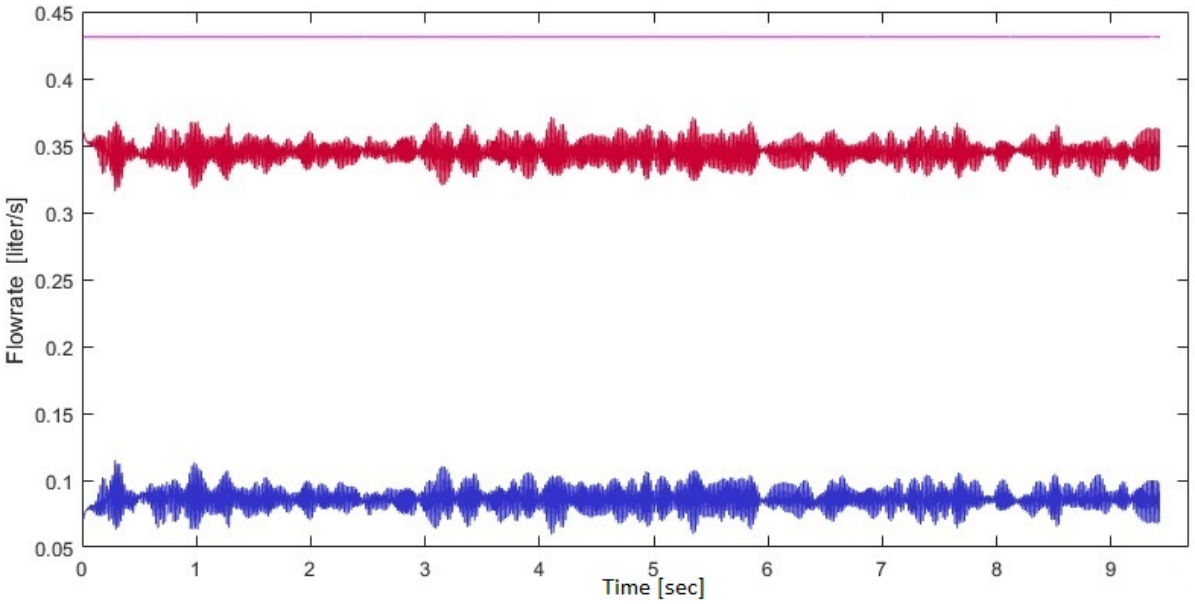

Figure 5.4: Flow rates at 20°C of water (blue), oil (red) and the imposed total flow rate (magenta).

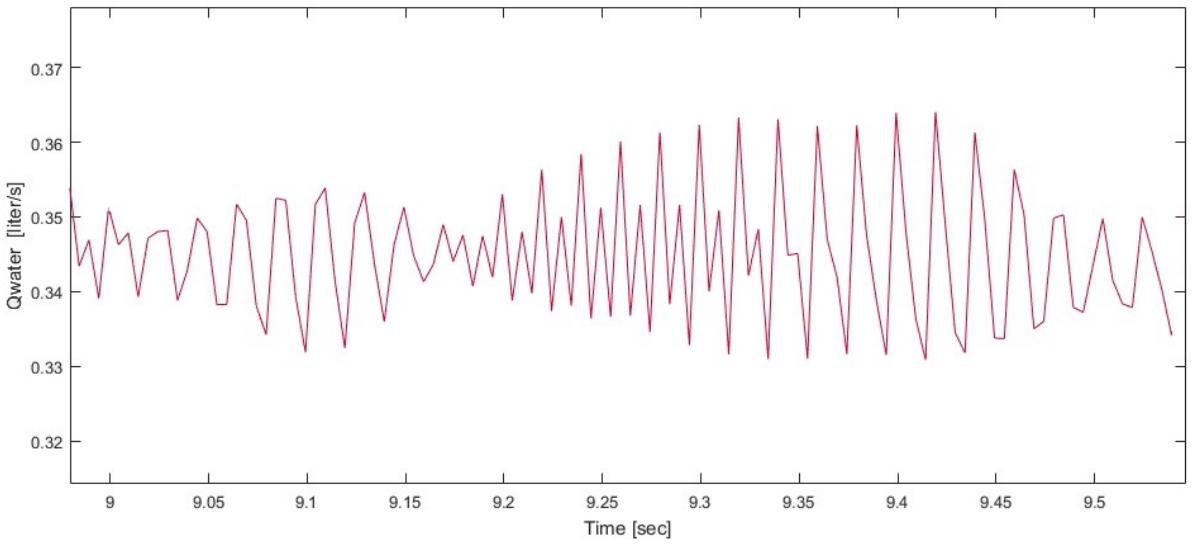

Figure 5.5: Zoom in of oil flow rate from 9 to 9.6 seconds. Sampling time is 0.005 sec.

The water flow rate shows the same behaviour as the oil flow rate, which is the consequence of the constant total flow rate. Obviously the water cut shows exactly the same behaviour as the water flow rate; see figure 5.6. When the numerical simulations are continued long enough over time, the average of fluctuations can be determined. When the average over a sufficient long time interval is taken the results are compared with the experiments. The numerical flow rates show a good comparison with the experiments. While for the experiment the water cut was 20.02% the water cut of the simulation is 19.94%.

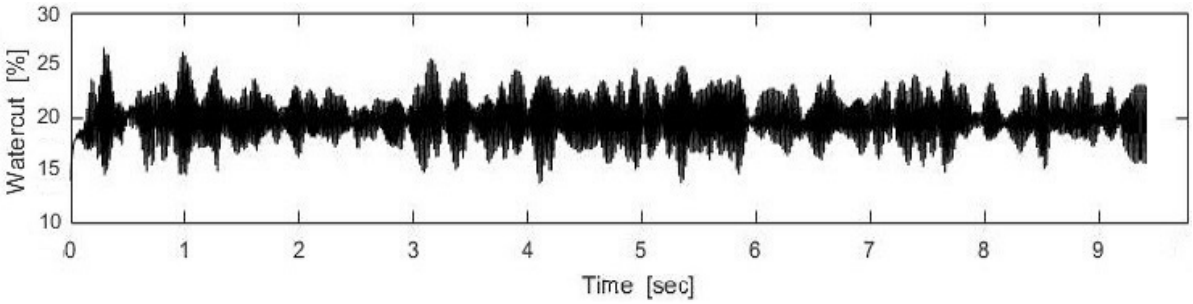

Figure 5.6: Water cut at 20°C. Sampling time is 0.005 sec.

For the used holdup fraction of 1.39 and the imposed total flow rate the simulation successfully simulated core-annular flow with a water cut of 19.94%, which is close to the value of 20.02% used in the experiments. The other important result is the pressure gradient in the pipe. The pressure gradient seems to stabilize between 2 and 3 seconds in figure 5.7. The averaged pressure gradient is then approximately 951 Pa/m. This is a 5% difference with the experiment which denotes a fairly good agreement. As the pressure gradient is also calculated at the right boundary the fluctuations are again visible. The pressure gradient however has a sampling time of $3 \cdot 10^{-6}$ seconds because it is calculated during every pressure-velocity coupling iteration. Therefore the small fluctuations are now smoother than for the flow rates.

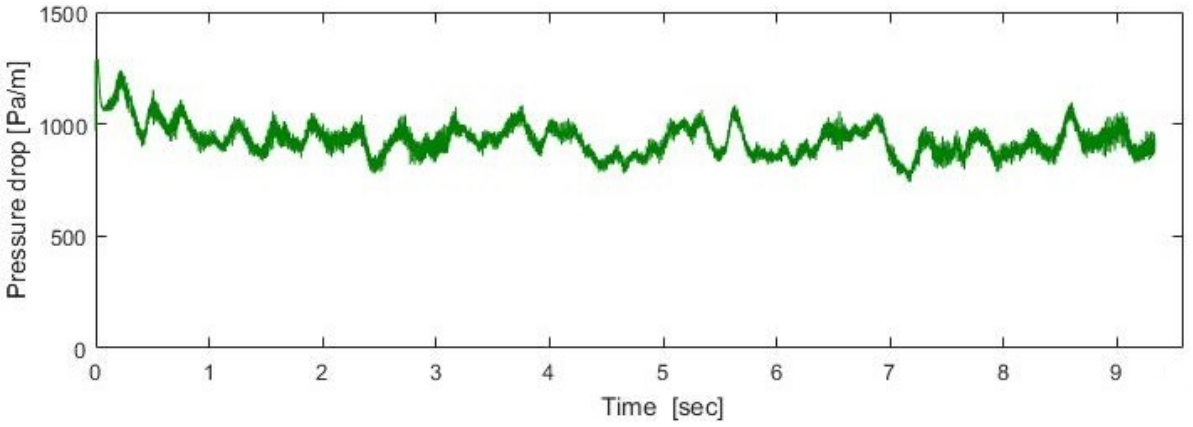

Figure 5.7: Pressure gradient at 20°C. Sampling time is $3 \cdot 10^{-6}$ sec.

As the key quantities in the simulations show a good agreement with the experiments the wave characteristics are studied. In figure 5.8 and 5.9 the non-dimensional amplitude 2.12a and water layer thickness 2.12b are plotted. These quantities are measured from a longitudinal cross-section as shown in figure 5.1. The strong irregular behaviour of the waves is clearly visible together with the eccentricity of the oil core. Also the expectation of larger waves at the bottom is again confirmed with these plots. The mean values are averaged over the same time interval as the pressure gradient. The scaled water thickness Tw is 0.098 at the top and 0.186 at the bottom. The scaled average amplitude A^* of the waves is 0.034 at the top interface and 0.075 at the bottom. The thickness of the water layer at the bottom is 1.90 times the value of the top. The waves at the bottom are 2.17 times as large as at the top. These are averaged values and the deviations from these values are quite high. Therefore it is important to run the simulation long enough to obtain representative values.

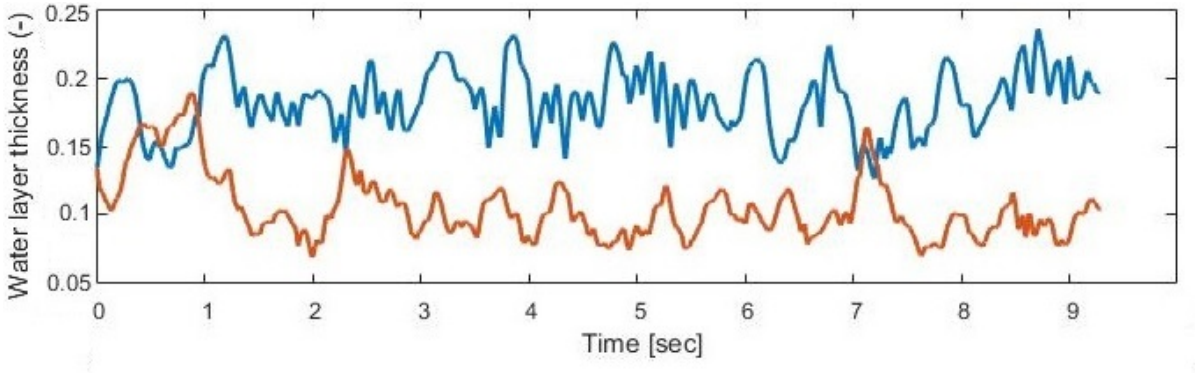

Figure 5.8: Scaled water layer thickness at the top (orange) and bottom (blue) for 20°C. Sampling time is 0.005 sec.

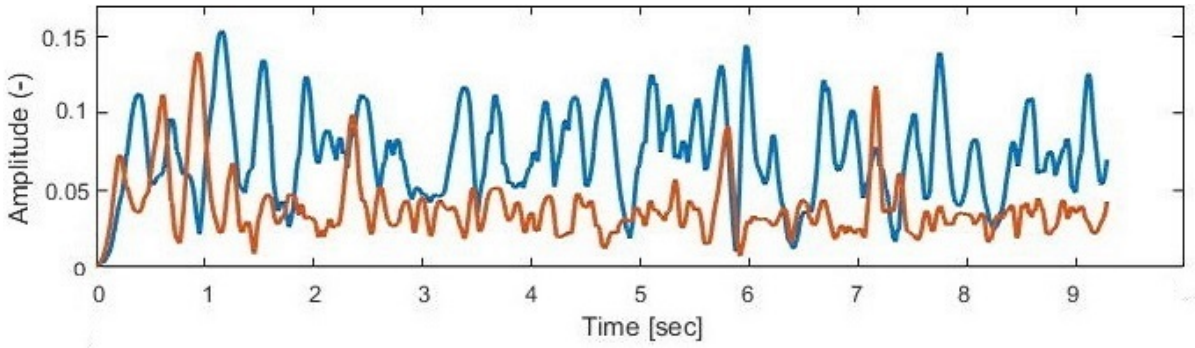

Figure 5.9: Scale wave amplitudes at the top (orange) and bottom (blue) interface for 20°C. Sampling time is 0.005 sec.

5.2. Simulation II: temperature 30°C (ν_0 = 1472 cSt)

Core-annular flow is found with irregular waves at the interface with two waves at the top interface and two at the bottom. The oil core looks more eccentric in figure 5.10 compared to the case with the higher oil viscosity at 20°C. The ratio between the turbulent viscosity and the molecular water viscosity again indicates only turbulence at the bottom, the ratio has increased with 50% to a maximum value of around 30; see figure 5.11.

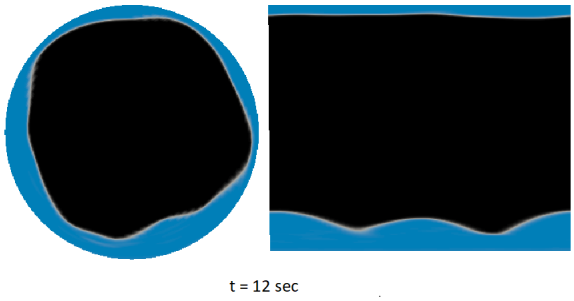

Figure 5.10: Cross-sections for the distribution of water (blue) and oil (black) at 30°C.

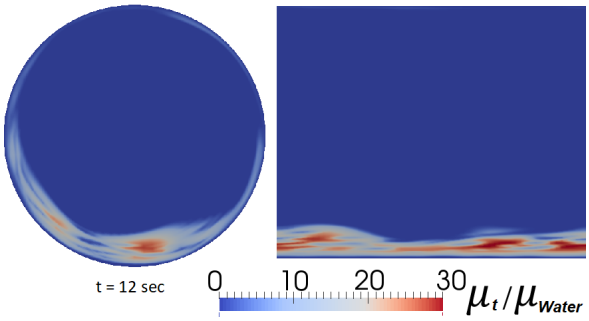

Figure 5.11: Ratio of the turbulent to molecular viscosity at 30°C.

The water cut as obtained in the simulation shows a small deviation with respect to the experimental value of 20%. As shown for the simulation in figure 5.12, the average value for the water cut from 0 to 3 seconds is 20% but from 3 to 8 seconds the water cut decreases. From 8 seconds on the water cut

is converged to an average value of 19.1%. This means that the flow rate of water is slightly lower. As the total flow rate is constant the oil flow rate in the simulation is higher than in the experiment. The holdup fraction in this simulation is the same as in simulation I, which means that the oil core is flowing slightly faster in this simulation II.

When the water cut at 3 seconds starts to deviate from 20% the pressure gradient also starts to change; see figure 5.13. The oil starts to flow faster and the velocity difference with the water increases. The viscous core is experiencing more resistance. From 8 seconds the water cut is converged and the pressure gradient stops increasing. The calculated pressure gradient for the converged situation is approximately 1215 Pa/m. This is a difference of 12% with the experimental result.

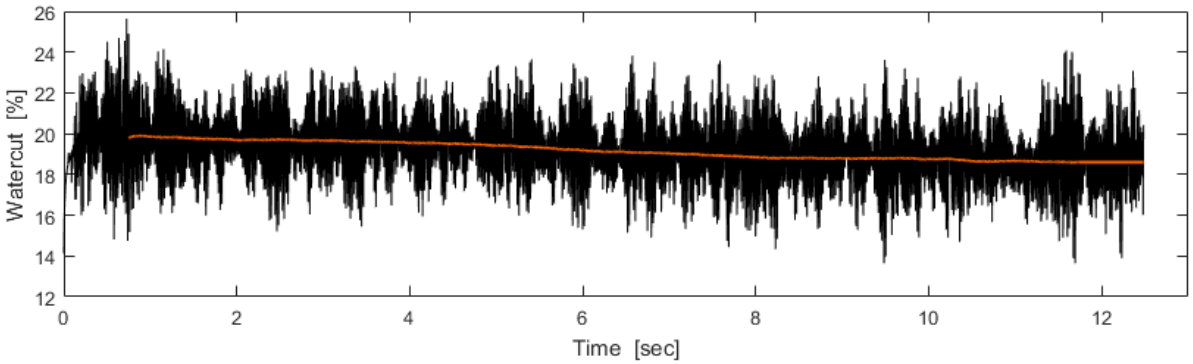

Figure 5.12: Water cut at 30°C. Orange line is the time average water cut for clarification. Sampling time is 0.005 sec.

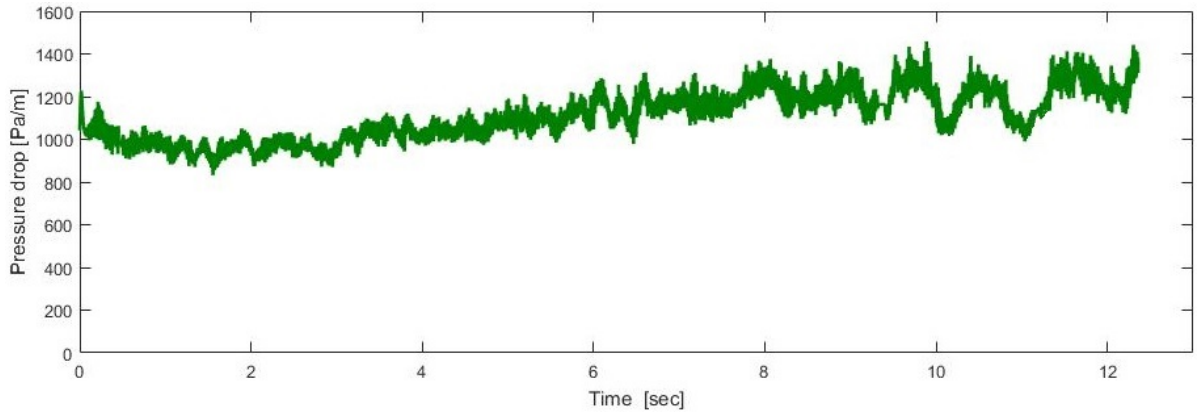

Figure 5.13: Pressure gradient at 30°C. Sampling time is $3 \cdot 10^{-6}$ sec.

Despite the 12% deviation of the pressure gradient with the experiment it is still interesting to look at the wave characteristics at the interface. Figures 5.14 and 5.15 show again the water layer thicknesses and the wave amplitudes. These calculations are made on a same slice through the pipe as was done for the 20°C case. From 3 until 8 seconds especially the interface at the bottom is varying with the changing water cut. The converged scaled water thickness Tw at the bottom interface is 0.254. The thickness of the top annulus changes slightly during this time interval and it finally obtains a scaled thickness of 0.080. The water annulus is 3.2 times thicker at the bottom compared to the top. Although the water layer at the bottom becomes larger, the top layer does not change much. The reason for this is that between 3 and 8 seconds the water layers at the left and right side of the pipe become smaller. The rising water layer at the bottom is compensated by decreasing water layers at the sides and not at the top. The levitation mechanism retains the core-annular flow pattern. The amplitude A^* of 0.087 at the bottom is 3.0 times the value of 0.029 at the top. Again strong deviations are present due the irregularity of the waves.

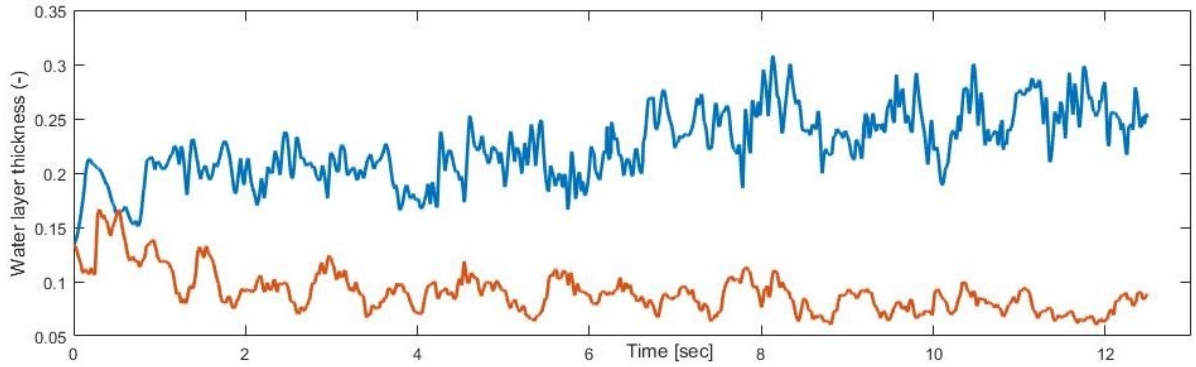

Figure 5.14: Scaled water layer thickness at the top (orange) and bottom (blue) for 30°C. Sampling time is 0.005 sec.

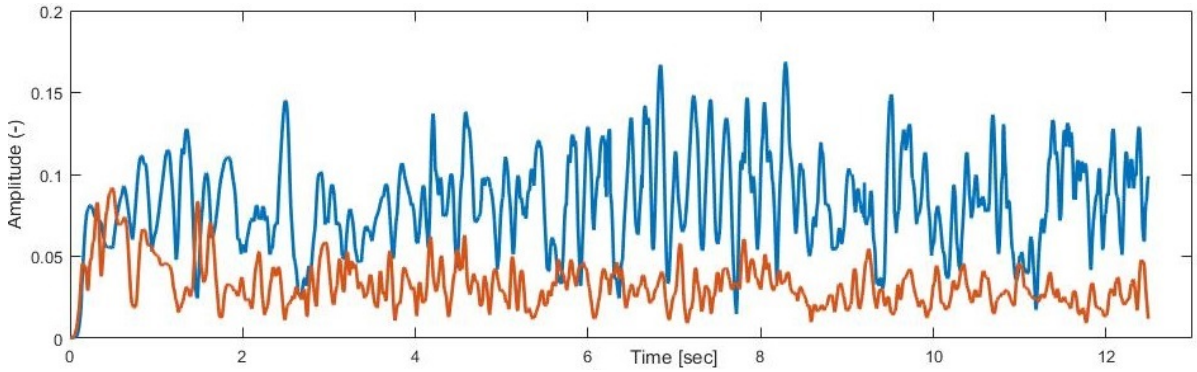

Figure 5.15: Scaled wave amplitudes at the top (orange) and bottom (blue) interface for 30°C. Sampling time is 0.005 sec.

5.3. Simulation III: temperature 40°C (ν_0 = 718 cSt)

The density ratio is similar to the value used in the previous simulations but the viscosity ratio is 2.7 times as large as for 20°C. Again core-annular is found in figure 5.16 with two to three waves at the top and bottom interface. The interface is more wavy than in the previous two simulations. At 12 seconds when the simulation is converged the eccentricity of the core is not very clear anymore. The turbulent to molecular viscosity ratio has values of 15 to 20 around the whole annulus; see figure 5.17. At the bottom a maximum value of 23 is found.

The water cut shows a similar behaviour as in the 30°C case, but now its value is even more different from the 20% water cut in the experiment. Until 2 seconds the water cut is 20% and thereafter it decreases to 16.8% at 10 seconds; see figure 5.18. Therefore is the oil flow rate higher than intended and the water flow rate lower. From figure 5.19 is seen that the pressure gradient strongly increases between 2 to 10 seconds and converges to a value of around 2830 Pa/m.

The waves at the interface show an interesting behaviour. Starting from perfect core-annular flow the core quickly becomes eccentric. The thickness of the water annulus at the bottom is larger than in the previous two simulations and the thickness at the top is smaller; see figure 5.20. After the waves on the interface are developed the core is moving down closer to the center. The scaled thickness of the water layer at the bottom decreases from approximately 0.25 to about 0.16. At the same time the thickness of the water layer at the top increases. The width of the oil core is reduced to compensate for the sharp decrease of the bottom annulus. Although figure 5.16 is a snapshot, this change in the core shape is clearly visible. The core is still eccentric, but not as much anymore as for simulations I and II. The amplitudes of the waves change together with the changing water thicknesses; see figure 5.21. At the bottom interface the waves show large variations but when the interface has been moved to the wall the amplitude of the waves becomes smaller and less varied. The converged thickness of the annulus at the bottom is 1.47 larger than at the top and the amplitudes at the bottom are 1.44 times larger than at the top.

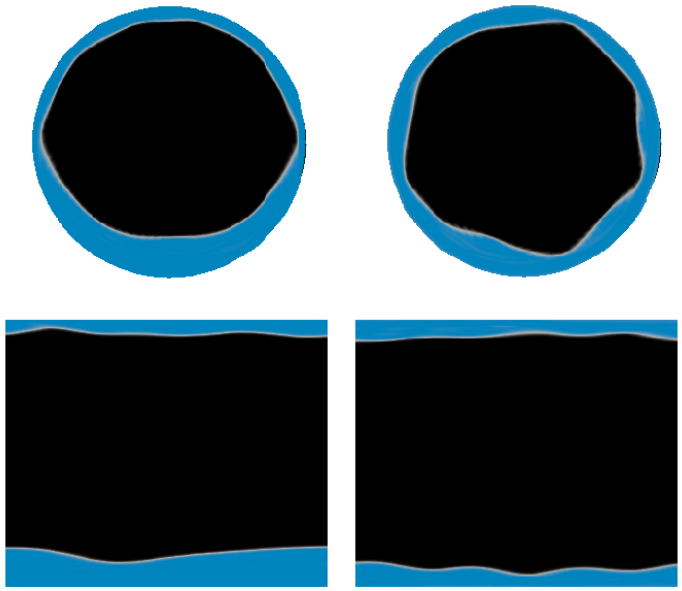

Figure 5.16: Cross-sections for the distribution of water (blue) and oil (black) at 40°C.

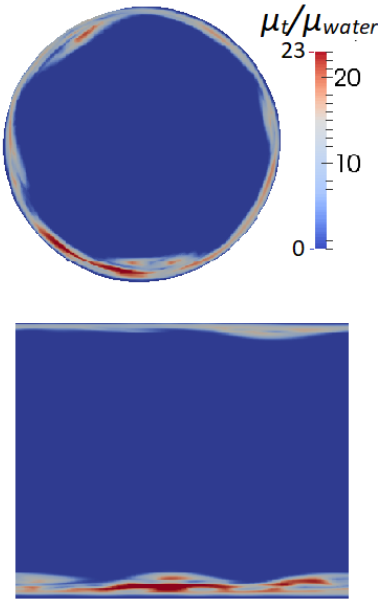

Figure 5.17: Ratio of the turbulent to molecular viscosity at 40°C.

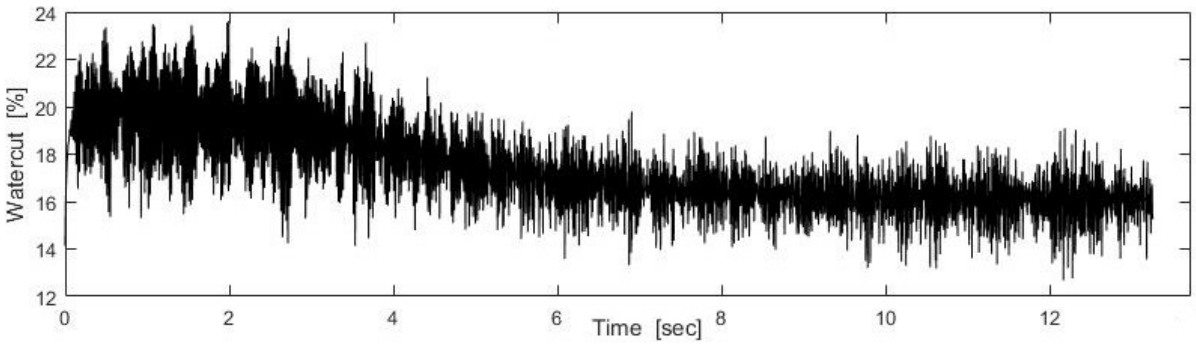

Figure 5.18: Water cut for 40°C. Sampling time is 0.005 sec.

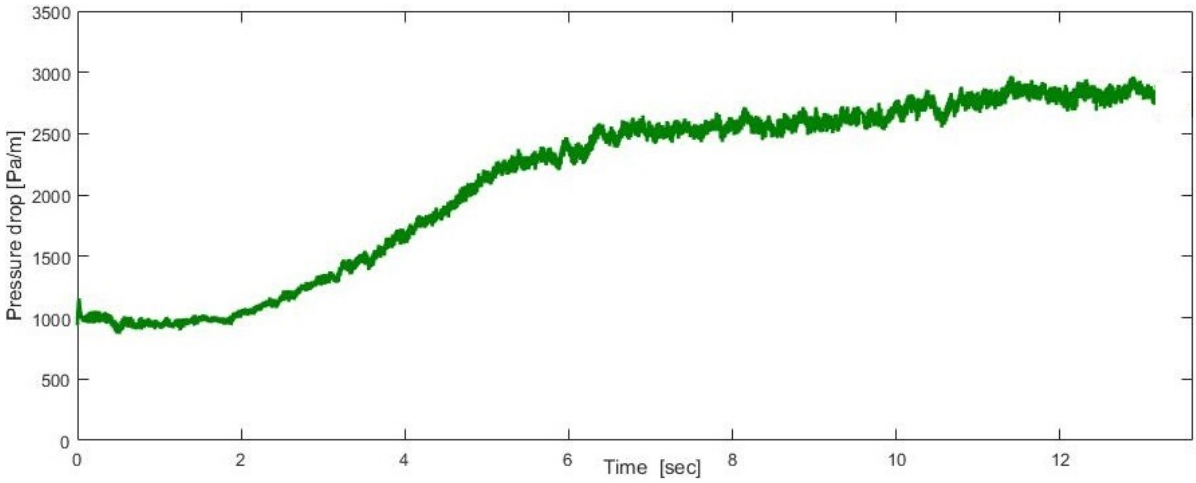

Figure 5.19: Pressure gradient for 40°C. Sampling time is $3 \cdot 10^{-6}$ sec.

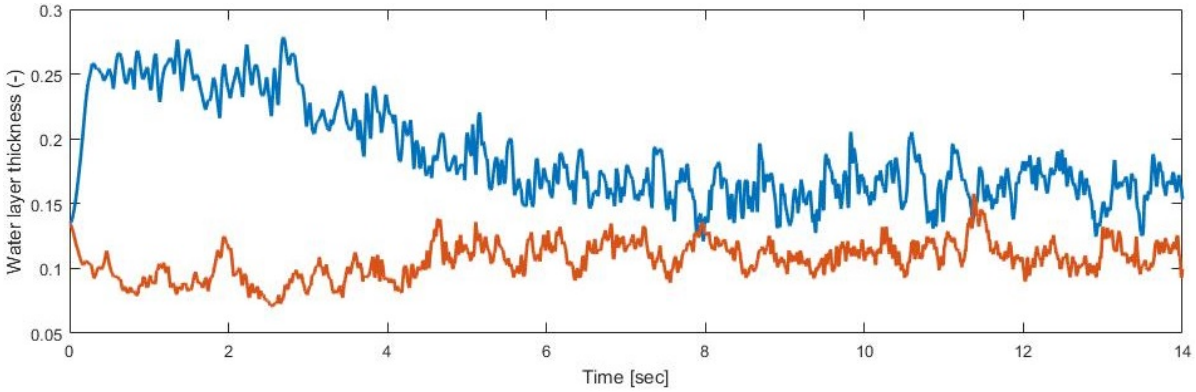

Figure 5.20: Scaled water layer thickness at the top (orange) and bottom (blue) for 40°C. Sampling time is 0.005 sec.

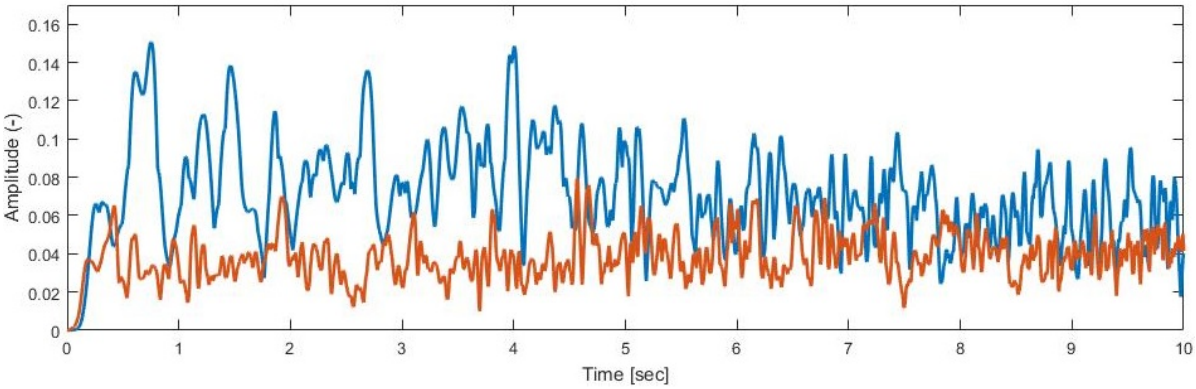

Figure 5.21: Scaled wave amplitudes at the top (orange) and bottom (blue) interface for 40°C. Sampling time is 0.005 sec.

5.4. Simulation IV: temperature 50°C (ν_0 = 383 cSt)

The numerical simulation failed to reproduce core-annular flow in contrast to the experiment. Similarly as in the 40°C simulation the core directly becomes very eccentric. From the cross-sections it is seen that at 1 second the waves at the interface are no longer present; see figure 5.22. The levitation mechanism is based on the shape of the waves and as these are absent the oil is fouling the pipe wall. A Kelvin-Helmholtz instability is found during the transition from core-annular flow to stratified flow. At 8 seconds the stratified flow regime is visible but still with some water at the top of the pipe. It is expected that for longer simulation time all the water will settle at the bottom of the pipe. The turbulent to molecular viscosity ratio shows values around 95 in the water layer; see figure 5.23. This is the same result as when water would flow through the pipe as a single phase flow. For stratified flow the water is more turbulent than for core-annular flow.

The effect of fouling is also visible in the simulation results for the water cut and the pressure gradient in figures 5.24 and 5.25. When the oil touches the pipe wall the lubrication layer disappears. Due the high viscosity of oil the resistance of the flow largely increases. The flow rate of oil decreases and therefore the water flow rate increases to maintain the total flow rate constant. The water cut increases very quickly during the fouling and it reaches a value of approximately 32%. With the absence of the lubrication layer the pressure gradient increases to 15250 Pa/m and probably even to a higher value if the simulation is extended longer in time. The simulation is not yet converged to a completely stratified flow but as the core-annular flow is already gone it is very unlikely that the flow can return to the core-annular flow pattern.

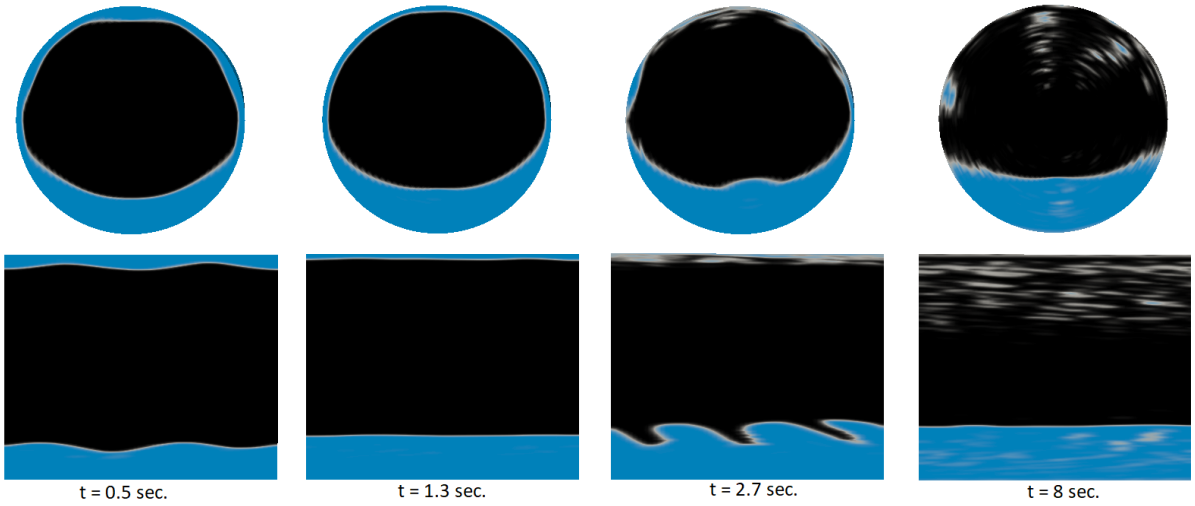

Figure 5.22: Cross-section and longitudinal cross-section for the distribution of water (blue) and oil (black) at 50°C.

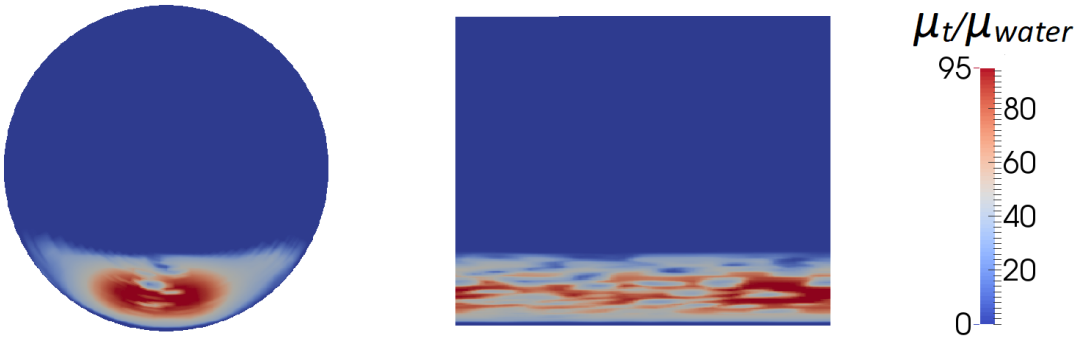

Figure 5.23: Ratio of turbulent viscosity to the molecular viscosity at 50°C.

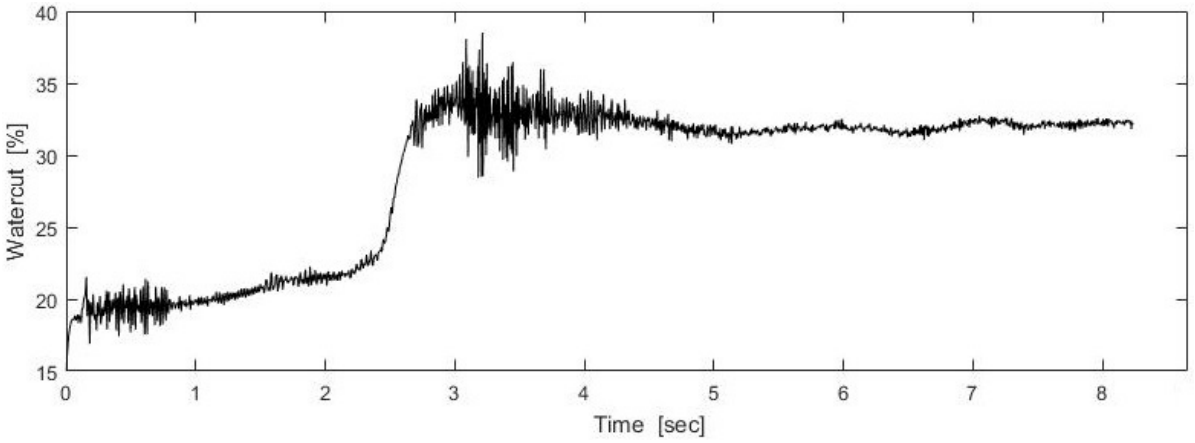

Figure 5.24: Water cut at 50°C. Sampling time is 0.005 sec.

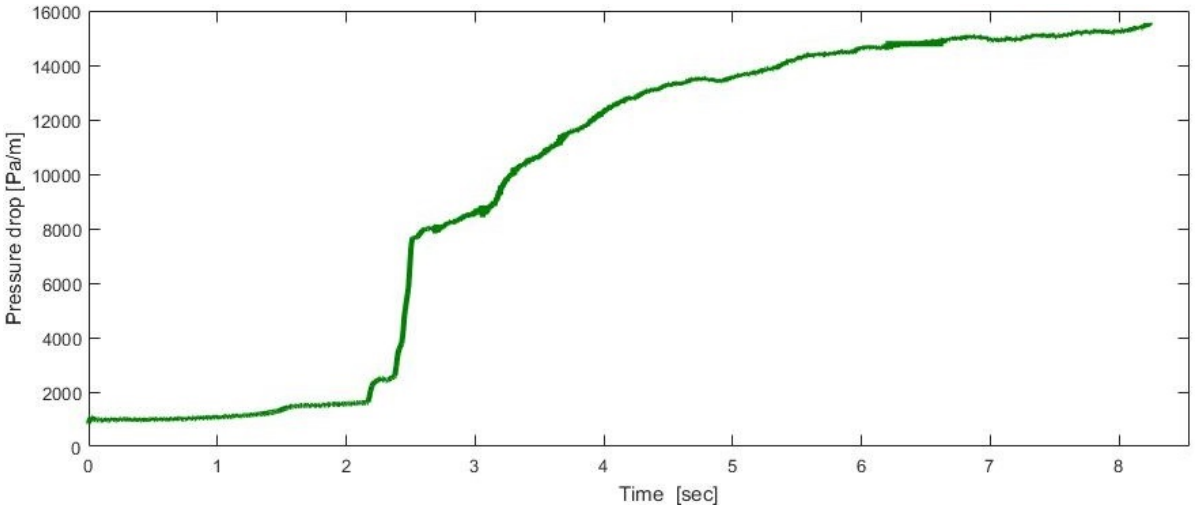

Figure 5.25: Pressure gradient at 50°C. Sampling time is $3 \cdot 10^{-6}$ sec.

5.5. Overview

Four experiments with a watercut of 20% were simulated with OpenFOAM. Each of the cases has a different temperature, which means a different oil viscosity. The simulations were performed with an imposed total flow rate of $0.430 \cdot 10^{-3}$ m^3/s. The imposed oil holdup fraction was taken the same in the 4 cases, namely 0.749. For 20°C the water cut that is found as a result of the simulation is similar with the experimental value of 20%. The pressure gradient for this case deviated 5% with the experimental value. For the simulations at 30°C and 40°C the water cut is deviating from 20% which also leads to differences between the numerical pressure gradient and the measured experimental pressure gradient. The 50°C simulation converged to the stratified flow pattern in contrast to the core-annular flow pattern that was found in the experiment. To try obtaining a value of the water cut closer to 20% in the simulations for the higher temperatures (i.e. lower oil viscosities), additional simulations need to be carried out that impose a different value for the oil holdup fraction.

The amplitude of the waves show a dependency on the thickness of the water layers. For larger water layers the waves have more space to grow. For smaller water layers the amplitudes of the waves become smaller. The position of the core influences the shape of the waves and also has a strong influence on the water cut and pressure gradient. It is found that similar with the eccentricity the watercut and pressure gradient changes. All properties are thus highly interdependent.

In table 5.2 all the results of the simulations are collected. Besides the interface on the top and bottom also the characteristics of the interface at the left and right are included for completeness.

Table 5.2: Overview of the results of the simulations I to IV.

Simulation		**I**	**II**	**III**	**IV**
Temperature		20°C	30°C	40°C	50°C
Oil viscosity	[cSt]	3338	1472	718	383
Qtotal	$\cdot 10^{-3}$ [m^3/s]	0.430	0.430	0.430	0.430
Oil holdup	[-]	0.749	0.749	0.749	0.749
Water holdup	[-]	0.251	0.251	0.251	0.251
Flow properties					
Water cut	[%]	19.9	19.2	16.8	32.2
$(\mu_t/\mu_w)_{max}$	[-]	19	30	23	95
Pressure gradient:					
- Simulation	[Pa/m]	951	1215	2829	15240
- Experimental	[Pa/m]	1004	1086	1123	1045
Water thickness Tw [-]					
Left		0.134	0.115	0.132	x
Right		0.131	0.117	0.129	x
Top		0.098	0.080	0.113	x
Bottom		0.186	0.254	0.166	x
Amplitude A^* [-]					
Left		0.050	0.046	0.047	x
Right		0.050	0.045	0.048	x
Top		0.034	0.029	0.041	x
Bottom		0.075	0.087	0.059	x
Ratios [-]					
Tw - Right/Left		0.98	1.01	0.98	x
Tw - Bottom/Top		1.90	3.18	1.47	x
A^* - Right/Left		1.02	0.98	1.02	x
A^* - Bottom/Top		2.17	2.97	1.44	x

6

Numerical accuracy

The simulation times for obtaining the results described in the previous chapter were quite long. To optimize the computational effort a study for the used mesh is performed. First the meshes are described followed by their influence on the pressure drop and on the interface shape. Furthermore the application solvers from section 4.7 are compared with special attention for their simulation time.

6.1. Mesh description

When solving core-annular flow with CFD the continuous solution is approximated by discrete values in numerical control volumes. All the control volumes together are called the mesh or the grid. With an increase in the number of applied control volumes the accuracy of the numerical solution will improve. Above a certain number of volumes the results will hardly change anymore. This means that the mesh is fine enough to capture all the details of the flow and the solution is mesh independent. Increasing the number of volumes, however, will increase the required computational time. An optimum mesh of the problem would be a mesh with as little computational cost as possible while still giving a sufficiently accurate numerical solution.

On every control volume a solution will be calculated with the iterative schemes of chapter 4. If the total number of volumes decreases by a factor of two the number of floating point operations will also go down by approximately a factor of two. Besides this advantage, the increased control volume sizes also have an effect on the Courant number. This number is inversely proportional to the volume size. So for larger volumes a larger time step is allowed for the same Courant number restriction. Because the largest flow velocity is in the direction of the pipe length the volume sizes in this direction probably have the largest influence on the time step.

Solutions on 17 different meshes were obtained and they are all denoted by a different letter in table 6.1. The name 'Org' refers to the original mesh as used in chapter 5, which was taken from the work of Radhakrishnan [6]. All other meshes can be divided into three different categories. For meshes D and E only the influence of the volume size in the radial direction is tested. The number of volumes in the main flow direction and in the perimeter direction are kept the same with respect to the original mesh. For the other meshes until letter L the number of volumes in the radial direction is kept the same, but the number is changed in the main flow direction and perimeter direction. The last category contains the meshes L to Q. The concentrations of volumes should be increased in areas with larger gradients in the solution. For the specific case of core-annular flow this means a fine mesh at the interface and a coarse mesh at the core. The volume sizes in the radial direction at the interface are still the same, but in the center of the pipe the volumes are larger. A reduction of a factor two in the radial direction is achieved with these meshes.

Table 6.1: Overview of the meshes used for the mesh dependence study.

Mesh	Total volumes	Number of volumes in direction of		
		Main flow	Perimeter	Radius
Org	527040	60	80	126
A	395280	45	80	120
B	303885	45	60	126
C	263520	30	80	126
D	304110	45	80	94
E	226710	45	60	94
F	202590	30	60	126
G	161160	30	48	126
H	135060	20	60	126
I	107440	20	48	126
J	110520	30	32	126
K	73680	10	32	126
L	67680	30	48	53
M	87900	30	60	53
N	101520	45	48	53
O	131850	45	60	53
P	225240	60	80	53
Q	410560	80	95	60

6.2. Pressure gradient verification

Simulation I at 20°C, ν_0=3338 cSt, is used to compare the simulation results obtained on the different meshes. To verify the accuracy of the solution the pressure gradient is considered as this is an important property of the flow. The results are presented in figure 6.1 with three different colors for the three different categories.

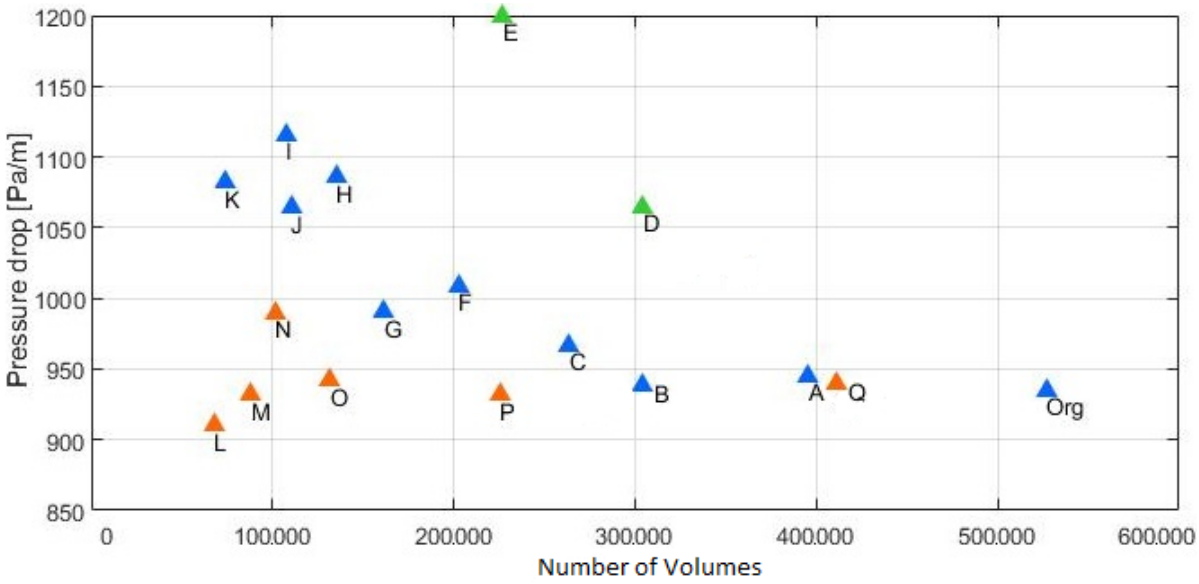

Figure 6.1: Pressure gradient results for simulation I for the different meshes of table 6.1.

Green category meshes

It is obvious that for a decrease in control volumes in the radial direction the pressure gradient significantly changes. For mesh E the pressure gradient is not even converged and still increasing. The interface is simulated too coarsely and from the visualizations it is seen that the interface is sometimes

spread over more than 8 to 10 volumes in the radial direction. For the original grid the volume of fluid method spreads the interface over 3 to 5 volumes. The water cut is decreased to 19.4% for mesh D and 18.8% for mesh E. The water cut of mesh D is however still decreasing.

Blue category meshes

For different lengths in the main flow direction and in the perimeter direction the solutions are more accurate. For meshes A and B the pressure gradient is similar with the original mesh while mesh B uses 1.7 times as few volumes. From mesh C the pressure gradient results starts to lose accuracy. For mesh A and B the water cut is 19.9% and 19.92% respectively. For meshes C to I the water cut decreases from 19.7% to 19.2%. A lower water cut means that the oil phase has a higher flow rate and water a lower flow rate. The increase in pressure gradient can be the result of the larger velocity difference which creates a larger shear stress along the interface. In the next section also the characteristics of the interface are studied.

Orange category meshes

For these meshes it is found that for 100000 volumes the pressure gradient results are fairly accurate. Meshes N and L show some deviation but mesh M gives fairly the same pressure loss as the original mesh. Mesh O has the same number of volumes in the main flow and perimeter directions as mesh B but now with coarser volumes in the core. In the same manner meshes F and M are similar except for the volumes in the core. A remarkable result is that mesh M looks accurate while mesh F does not. Mesh Q is created to check whether he original mesh is actually mesh independent. This mesh has more volumes than the original mesh. The pressure gradient was found to be almost the same as the original mesh which suggest that the original mesh is sufficiently reliable.

The purpose of this research is to find accurate results with as little volumes as possible. Although it follows from the pressure gradient verification of simulation I that mesh M is a good mesh, this has resulted in considerable different results for simulations II and III of chapter 5. To determine the cause of this, the influence of the meshes on the interfaces are studied.

6.3. Interface verification

In this section the shape of the interfaces are compared for the different meshes. From the pressure gradient verification already a selection could be made of which meshes do not work and can be excluded. Only mesh K is added for extra comparison. With respect to the interfaces, the wave amplitudes and the thickness of the water layers as obtained with the various meshes are compared with the results for the original mesh. The results are summarized in table 6.2.

Table 6.2: Absolute differences with respect to the 'Org' grid.

Mesh	**Amplitude** Upper Interface	**Amplitude** Lower Interface	**Water thickness** Upper Interface	**Water thickness** Lower Interface
Q	2%	-4%	-1%	2%
A	-1%	-9%	16%	-8%
B	-3%	-16%	18%	-13%
P	-2%	-5%	11%	-2%
O	-12%	-14%	11%	-6%
M	-24%	-34%	-2%	34%
K	-52%	-66%	-4%	43%

Grid Q has many volumes in the main flow and perimeter directions and it is found that the interfaces have similar properties as found with the original grid. Still some very small differences are found which are partly due to how these results are obtained from the simulation. A slice is taken in the longitudinal direction and then the average thickness value is taken over some time interval. By choosing slightly different time intervals small deviations can occur.

For the other meshes larger differences are found. All the amplitudes have a negative difference which means that the amplitudes are all simulated to be smaller than the values found on the original

mesh. By taking less volumes the waves are flattened on the interface. Despite the smaller waves still core-annular flow is found. The difference in the water thickness is alternately positive and negative for the upper and lower interface. When the water thickness at the top is smaller, the water thickness at the bottom is larger, and vice versa. This makes sense since the volumes of oil and water are constant during a simulation. Although this does not seem to hold for at least mesh M and K. The amplitudes of the waves are so small that the oil is settled differently in the pipe. The increasing lower interface is compensated by a smaller water layer thickness at the left and right side of the pipe. As the water thickness at the top is smaller than at the bottom this thickness shows a larger difference when expressed as a percentage.

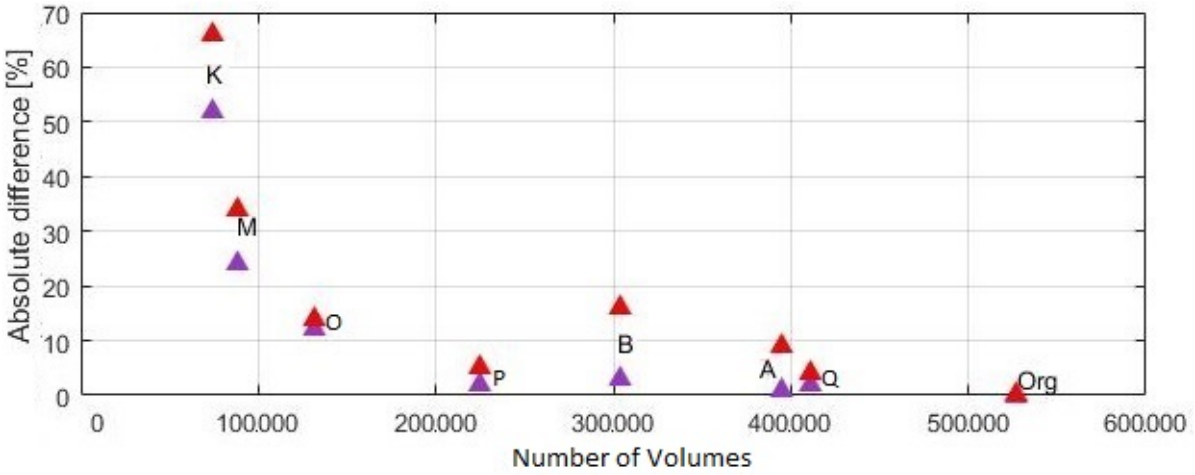

Figure 6.2: Absolute differences of amplitudes at the bottom interface (purple) and upper interface (red).

Figure 6.2 gives an overview of the accuracy of the amplitudes of the meshes from table 6.2. On the vertical axis the absolute values of the differences are displayed. While for mesh M the pressure result is accurate for the 20°C case, the interface looks different. From the interface comparison mesh P seems to be the best choice. In contrast to mesh M this mesh also shows a good agreement with simulations II and III of chapter 5. As displayed in figure 6.3 mesh M follows the same behaviour but in the simulation the increase in pressure is smaller. For 20°C the pressure gradient was not changing much after the start so this deviation was not found. In mesh P the number of volumes is decreased by a factor of 2.34. As the Courant number is mainly dependent on the volume sizes in the main flow direction the required time steps are still similar. Mesh P will from now on be used for all further numerical simulations.

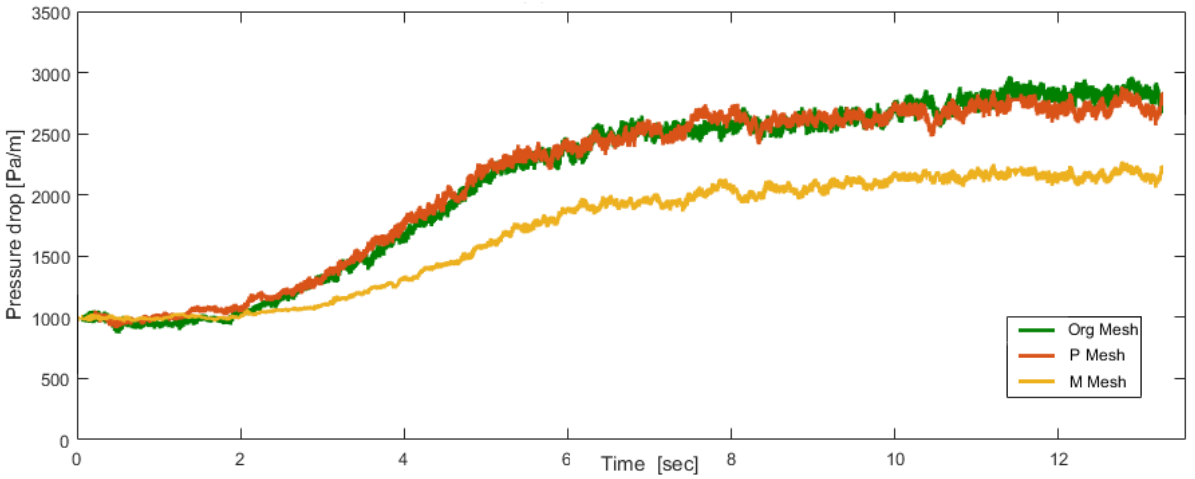

Figure 6.3: Pressure gradient results of mesh Org, P and M for simulation III.

6.4. Comparison of solvers

In contrast to the flux imposed solver, which keeps the imposed total flow rate constant, the pressure gradient solver provides the flow rate as output result. Simulation III is used to test the performance of the constant pressure gradient solver. The flux imposed solver for simulation III gave a pressure gradient of 2830 Pa/m and a water cut of 16.8% for a fixed flow rate of $0.430 \cdot 10^{-3}$ m^3/s. Using the same physical properties, the pressure gradient solver is run for an imposed pressure gradient of 2830 Pa/m. The total flow rate behaviour during that simulation is shown in figure 6.4. At the start the oil core is concentric and the interface is smooth. As there are no waves the phases can flow more easily and the total flow rate increases. At the point where the core is more eccentric and waves start to develop more accumulation occurs. The total flow rate starts to decrease. When the core height and waves are settled the total flow rate is $0.445 \cdot 10^{-3}$ m^3/s. This flow rate is quite close the imposed flow rate of $0.430 \cdot 10^{-3}$ m^3/s for simulation III. The found water cut is 16.6% versus the 16.8% water cut from simulation III.

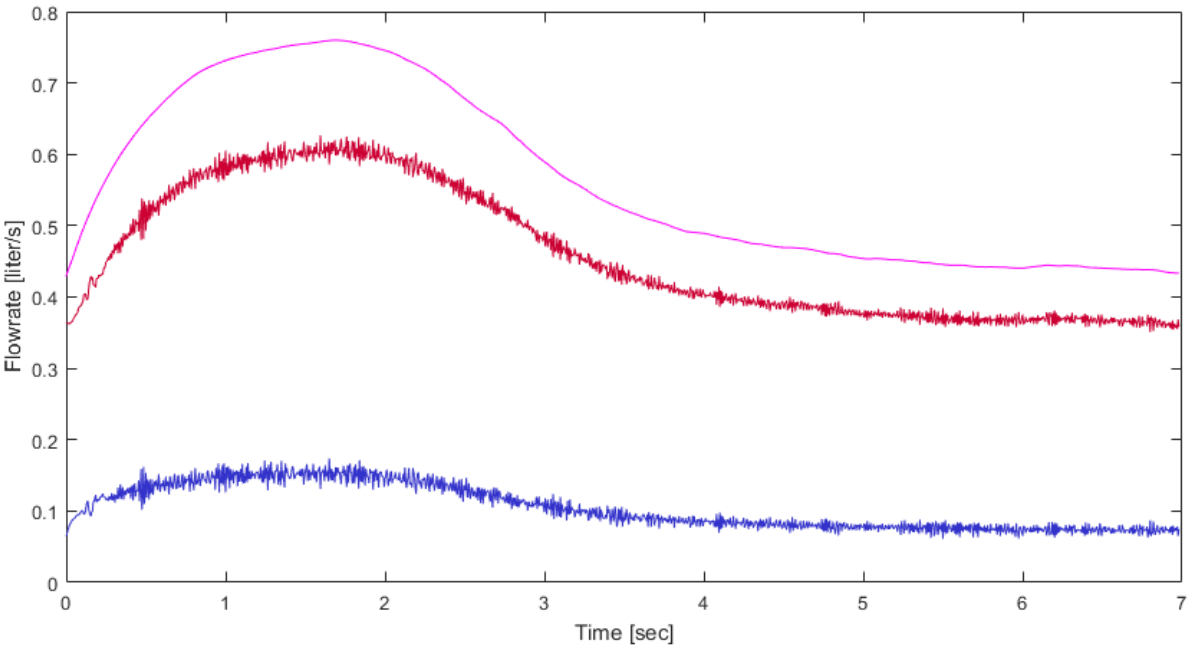

Figure 6.4: Simulation III repeated with the pressure gradient solver. Shown are the water flow rate (blue), oil flow rate (red) and the total flow rate (magenta).

The first difference which is noticeable is that for the flux imposed solver the simulation was converged after around 12 seconds whereas the pressure gradient solver seems to be converged after around 6 seconds. The flux imposed solver is dependent on the waves passing through the right periodic boundary. For the pressure gradient solver only the fluctuations for the irregular wave amplitudes are present. The removal of this dependency results is a much quicker convergence for the pressure gradient solver. It is found that for other simulations with the pressure gradient solver the convergence time is between 6 and 10 seconds. The pressure gradient solver has another advantage compared with to the flux imposed solver. During every pressure-velocity coupling iteration in the flux imposed solver the pressure is calculated that is required to keep the total flow rate constant. These iterations are not needed in the pressure gradient solver. This resulted in an extra time advantage of around 15%. The required iterations for the other variables from table 4.3 are similar.

6.5. New decomposition

As a new grid is going to be used with a new application solver, namely the pressure gradient solver instead of the flux imposed solver, the problem will have a different efficiency when computing in parallel mode. Thus the speedup and efficiency functions of section 4.8 are no longer valid. For mesh

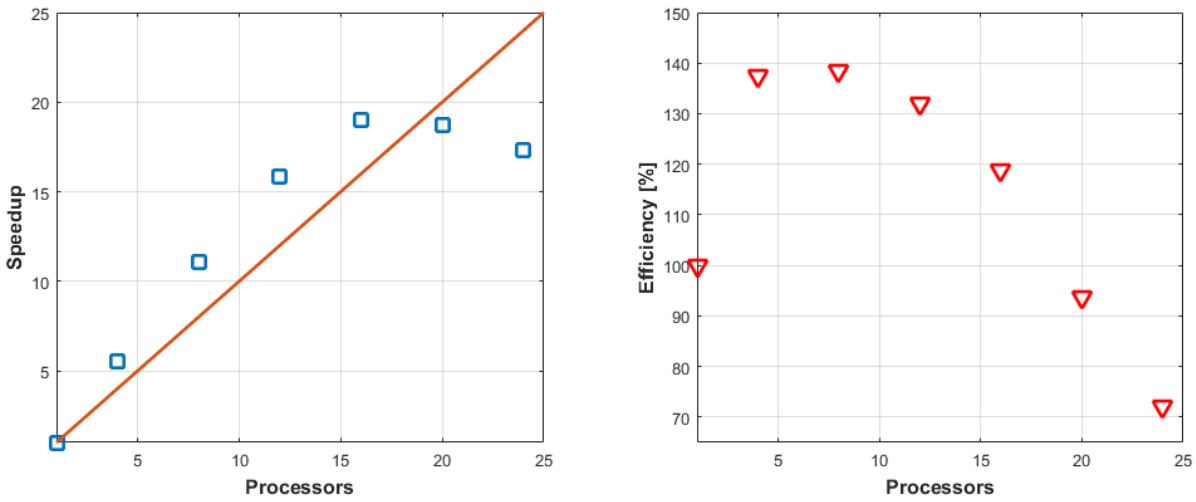

Figure 6.5: Speedup and efficiency function. Squares and triangles are the real measured data.

P the new functions are shown in figure 6.5. A large efficiency is achieved at 8 processors and the efficiency starts to decrease when more processors are used. The speedup is the largest between 16 and 20 processors and then starts to decrease. For the fastest calculations 16 processors should be used. As there are 28 processors available at one node the problems are solved with 14 processors. This improves the efficiency and 2 simulations at the same time can be solved at a single node.

6.6. Conclusion

It is found that fine control volumes close to the interface are required for obtaining accurate numerical solutions. However, a reduced computational time can be achieved by taking larger volumes in the center of the pipe. This has reduced the total number of volumes by a factor of 2.34 with a significant reduction in simulation time. For the new mesh one very important point of attention is that the interface at the bottom remains in the fine part of the mesh. When the water layer thickness at the bottom will increase too much and enters the coarse part of the mesh the results will directly lose accuracy.

From the comparison of the solvers it is found that the imposed flux solver and the pressure gradient solver give similar results. The pressure gradient solver, however, is more efficient. The switch to the flux imposed solver was done because it is more in line with how the conditions are imposed in the experiments. A new solver is desired in which both the oil flow rate and the water flow rate can be imposed, and in which the pressure gradient and the oil holdup are obtained as output results from the simulation. Without this, the solver with the imposed total flux is now not preferred due to the longer simulation time than the pressure gradient solver. With the new grid and the new solver the simulation time is reduced from 40 to 60 days in 15 to 25 days.

7

Numerical results for 40°C (ν_O = 718 cSt)

The numerical simulations presented in chapter 5 failed to correctly reproduce the experiments of van Duin at a water cut of 20%. For 20°C the simulation was in reasonable agreement with the experiments, but the results for higher temperatures (i.e. lower viscosities) were deviating too much. New simulations are performed in this chapter. The new grid of chapter 6 and the pressure gradient solver are used. The simulation of 40°C is tried to be improved by taking different phase holdups.

7.1. Results

For the simulation of 40°C of chapter 5, which is at a kinematic oil viscosity of 718 cSt, the oil and water volumes present in the simulated pipe section were initialized with a holdup ratio of 1.39. The corresponding holdup fraction of 0.749 converged to a water cut of 16.8%. The desired water cut of 20% is tried to be obtained by changing the initial amount of oil in the pipe. Water cut values of 9%,

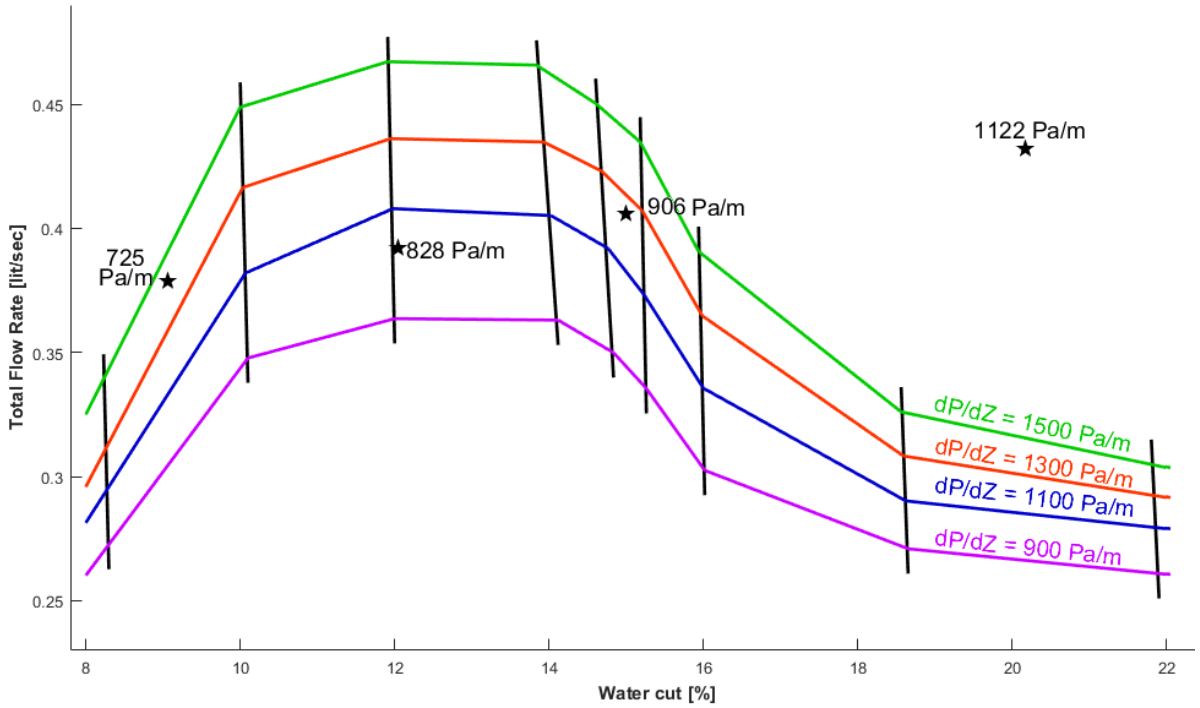

Figure 7.1: Water cut and total flow rate results for different holdup fractions (black lines) and pressure gradients (colored lines).

12% and 15% are also investigated since experiments at these water cuts also have been performed. Besides the different holdups also different pressure gradients are imposed. In figure 7.1 all the results are shown. Numerical simulations with nine different holdups and four different pressure gradients are done. The similar holdups are connected with black lines and the similar pressure gradients are connected with colored lines. With all the connections a grid is created which covers a solution region with the help of all the performed simulations. The experimental results are displayed with black stars in the figure.

By varying the oil holdup between 0.820 and 0.684 in the simulations a range of water cuts are found between 8.2% and 22%. For the same holdup and the different imposed pressure gradients small changes in the water cut are found. It is found that for higher pressure gradients the water cut decreases. The differences are however small. The corresponding initial oil holdups of the vertical black lines in figure 7.1 are given in table 7.1.

Table 7.1: Oil and water holdup fractions for the water cuts of figure 7.1.

Oil holdup [-]:	0.820	0.806	0.792	0.764	0.751	0.737	0.724	0.697	0.684
Water holdup [-]:	0.180	0.194	0.208	0.236	0.249	0.263	0.276	0.303	0.316
Water cut [%]:	~8.2	~10.1	~11.9	~14.0	~14.7	~15.2	~15.9	~18.6	~22.0

Along the constant pressure gradient curves larger differences are found. From a water cut of 8% the flow rate firstly increases followed by a decreasing flow rate after 14%. A maximum flow rate is found between a water cut of 12% and 14%. Using the created solution grid, numerical results at the experimental conditions for the water cut and total flow rate are estimated by linear interpolation within the covered solution region. A linear interpolation estimate is not possible for the experiment at a water cut of 20% as this experiment is outside the solution grid. For the other three experiments the numerical pressure gradients and oil holdups are interpolated for the same water cut and the same total flow rate values as the experiments.

Table 7.2: Linear interpolated numerical results from the solution grid of figure 7.1. The water cut and total flow rate values are similar with the experimental values.

Water cut	Qtotal	Pressure gradient		Oil holdup
9%	$0.379 \cdot 10^{-3}$ m^3/s	1434 Pa/m	(98% error)	0.814
12%	$0.392 \cdot 10^{-3}$ m^3/s	1028 Pa/m	(24% error)	0.792
15%	$0.406 \cdot 10^{-3}$ m^3/s	1240 Pa/m	(37% error)	0.772
20%	$0.430 \cdot 10^{-3}$ m^3/s	-	-	-

The numerical pressure gradient found at a water cut of 12% is the most accurate with 24% difference with the measured pressure gradient. At 15% water cut a difference of 37% is found and at a water cut of 9% the pressure gradient differs almost by a factor of two. An interpolation is not possible for the 20% water cut but this difference will be even larger.

In the following sections the flow properties will be studied more thoroughly for six different cases. Three simulations at imposed oil holdups of 0.820, 0.792 and 0.697 at a pressure gradient of 1100 Pa/m. At the imposed oil holdup of 0.792 also the other pressure gradients of 900,1300 and 1500 Pa/m are studied.

7.2. Interface comparison

Longitudinal cross sections for simulations with different holdup fractions are shown in figure 7.2 for a pressure gradient of 1100 Pa/m. The thickness of the water layers at the top look quite similar. Only the water layer for Ho=0.697 is a bit thicker than the other two. Larger differences for the various holdups are found at the bottom. Most of the extra water, due to the increased water cut, settles in the bottom layer. At Ho=0.820 the amount of oil in the pipe becomes so low that the difference between the top and bottom does not look very large anymore. For this holdup a water cut of 8% was found and the total flow rate was already strongly decreasing when the oil holdup was increased. In

the previous part of this report the statement was already made that the amplitudes of the waves are dependent on the thickness of the water layers. For all holdups therefore similar waves are found at the top. Two waves are found with approximately the same amplitudes. The wave amplitudes at the top layer of Ho=0.697 are a bit larger than those for the other two holdups. As the thickness of the water layers at the bottom show larger differences, the wave shapes are different. For the oil holdup of 0.820 three waves are visible, two waves for the oil holdup of 0.792 and one wave for the oil holdup of 0.697. All wave characteristics are summarized in table 7.3. For the same holdup, but different pressure gradients, there are small differences in the wave characteristics.

Figure 7.2: Longitudinal cross section for simulations with different holdup fractions at a pressure gradient of 1100 Pa/m.

Table 7.3: Interface results of simulations V to X.

Simulation	**V**	**VI**	**VII**	**VIII**	**IX**	**X**
Oil holdup [-]	0.820	0.792	0.792	0.792	0.792	0.697
Water holdup [-]	0.180	0.208	0.208	0.208	0.208	0.303
Water cut [%]	8.24	12.01	11.98	11.95	11.92	18.62
Pressure gradient [Pa/m]	1100	900	1100	1300	1500	1100
Water thickness Tw [-]						
Left	0.090	0.087	0.087	0.082	0.080	0.133
Right	0.095	0.086	0.084	0.083	0.082	0.140
Top	0.073	0.064	0.061	0.062	0.061	0.099
Bottom	0.127	0.230	0.229	0.237	0.234	0.289
Amplitude A^* [-]						
Left	0.027	0.030	0.032	0.028	0.024	0.057
Right	0.025	0.029	0.031	0.029	0.024	0.056
Top	0.018	0.016	0.018	0.017	0.015	0.038
Bottom	0.041	0.063	0.070	0.074	0.069	0.101
Ratios [-]						
Tw - Right/Left	1.06	0.99	0.96	1.01	1.00	1.05
Tw - Bottom/Top	1.76	3.69	3.73	3.82	3.80	2.91
A^* - Right/Left	0.93	0.96	0.98	1.03	1.00	0.99
A^* - Bottom/Top	2.26	3.90	3.95	4.40	4.65	2.65

7.3. Ullmann & Brauner model

The experimental and numerical results are compared with the predictions from the model [24] described in section 2.5. The model predicts the pressure gradient and holdup for certain oil and water flow rates. The numerical results described in this chapter are performed with the pressure gradient solver. The Ullmann & Brauner model is therefore also iteratively solved for a given pressure gradient at various values of the oil holdup fraction. Figure 7.3 shows the flow rate results from the Ullmann &

Brauner model and from the numerical simulations. All results are obtained for a pressure gradient of 1100 Pa/m. The numerical simulations results are only available between a water cut of 8% and 23%.

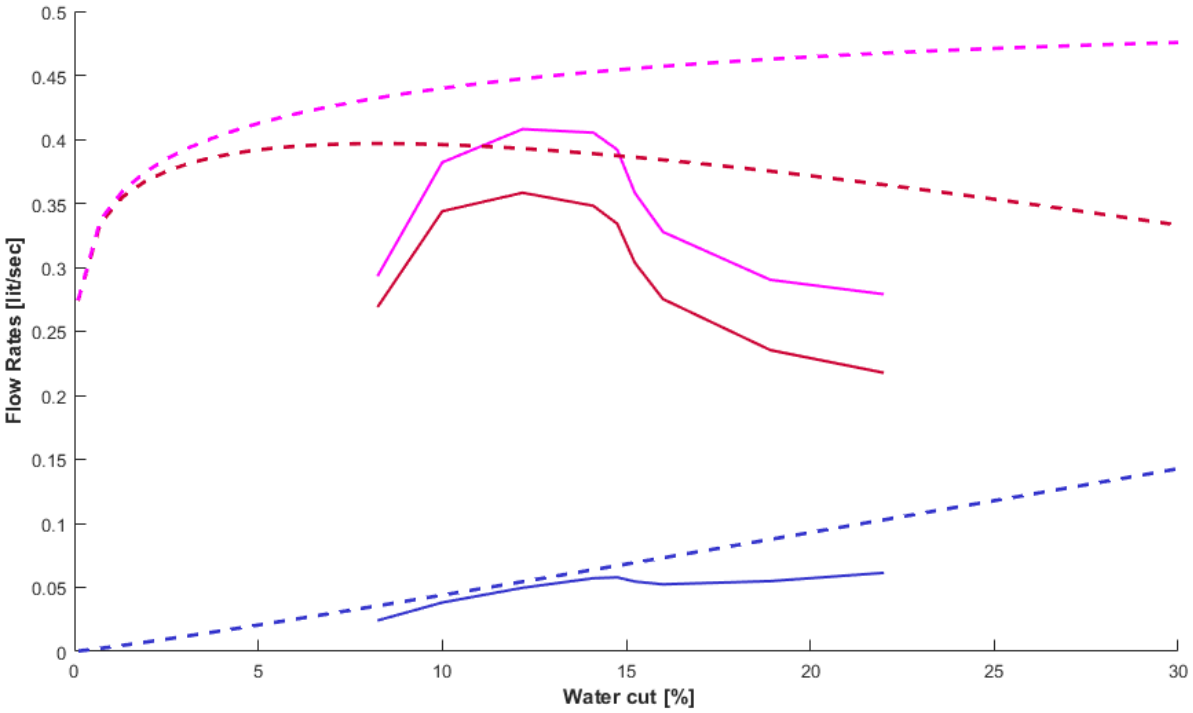

Figure 7.3: Numerical results (solid lines) and predictions with the Ullmann & Brauner model (dashed lines) at various values of the oil holdup fraction at a pressure gradient of 1100 Pa/m. Water flow rates are blue, oil flow rates are red and the total flow rates are represented with the magenta color.

Some remarkable differences are found between the Ullmann & Brauner model and the numerical simulations. In particular below a water cut of 11% and above 14% the differences are large. Above 14% the numerical water flow rates increase less quickly than the predicted water flow rate. At the same time the numerical flow rate of oil decreases much faster than the predicted oil flow rate. The numerical oil flow rate decreases so fast that the total flow rate also decreases. The Ullmann & Brauner model, however, still predicts an increase of the total flow rate. All performed experiments show a similar behaviour as the Ullmann & Brauner model, which indicates that the error is in the numerical simulations.

In the numerical simulations thicker water layers are found at the bottom when the oil holdup is reduced. Thicker water layers at the bottom resulted in a smaller number of waves with larger amplitudes. For Ho=0.820 there are three waves at the bottom interface while for Ho=0.697 there is only one. At a holdup of 0.751, alternately one and two waves are visible. When decreasing the oil holdup further, and increasing the water cut, the number of waves at the bottom is one. There is a large difference in amplitude size between one and two waves and the resistance between the oil and water phase is increased too much as compared to the experiments. It thus seems that the domain length has a too large influence on the results when the number of waves in the domain becomes lower than two.

Below 10% water cut, with the fixed pressure gradient, the numerical flow rates decrease strongly when the water cut is reduced. This strong decrease for the Ullmann & Brauner model is only predicted below a water cut of about 2.5%. This difference can be due to inaccuracies in the Ullmann & Brauner model and the numerical results. The Ullmann & Brauner model still predicts a quite high flow rate at a water cut of 2.5%, while in reality it is unlikely that core-annular flow can exist for such a low water cut. The model is less accurate for water cuts below 10%. From table 7.2 it is, however, also found that the numerical simulations become less accurate at a water cut of 9%. No experiments are

performed below a water cut of 9%, but as the water cut goes to 0% the total flow rate should go to almost 0 m^3/s. At 0% water cut only the very viscous oil is present in the pipe which is too viscous to be driven by pressure gradients of 900 to 1500 Pa/m. The predications with the Ullmann & Brauner model and the numerical results both have their inaccuracies below a water cut of 10%. The behaviour of the experiments will lie somewhere in between.

In table 7.4 the predictions of the Ullmann & Brauner model are shown for exactly the same water cut and flow rates of the experiments performed at 40°C. At water cuts of 12% and 15% the predictions match the experiments very well. At 9% water cut the model over predicts the pressure gradient and at 20% water cut the model underestimates the pressure gradient. All the errors fall within an accuracy interval of 20%.

Table 7.4: Predictions with the Ullmann & Brauner model for the experiments at 40°C.

Water cut	Qtotal	Pressure gradient		Oil holdup
9%	$0.379 \cdot 10^{-3}$ m^3/s	856 Pa/m	(18% error)	0.894
12%	$0.392 \cdot 10^{-3}$ m^3/s	872 Pa/m	(5% error)	0.860
15%	$0.406 \cdot 10^{-3}$ m^3/s	896 Pa/m	(-1% error)	0.828
20%	$0.430 \cdot 10^{-3}$ m^3/s	964 Pa/m	(-14% error)	0.772

Figure 7.4 also shows the solutions of section 7.1 and the curves obtained at constant pressure gradient obtained with the Ullmann & Brauner model. The same imposed pressure gradient values are used in the Ullmann & Brauner model as for the numerical simulations, indicated with the same colors. For all different pressure gradients the same differences are found below the water cut of 11% and above the water cut of 14%. The Ullmann & Brauner model predicts the pressure gradients better than the numerical simulations.

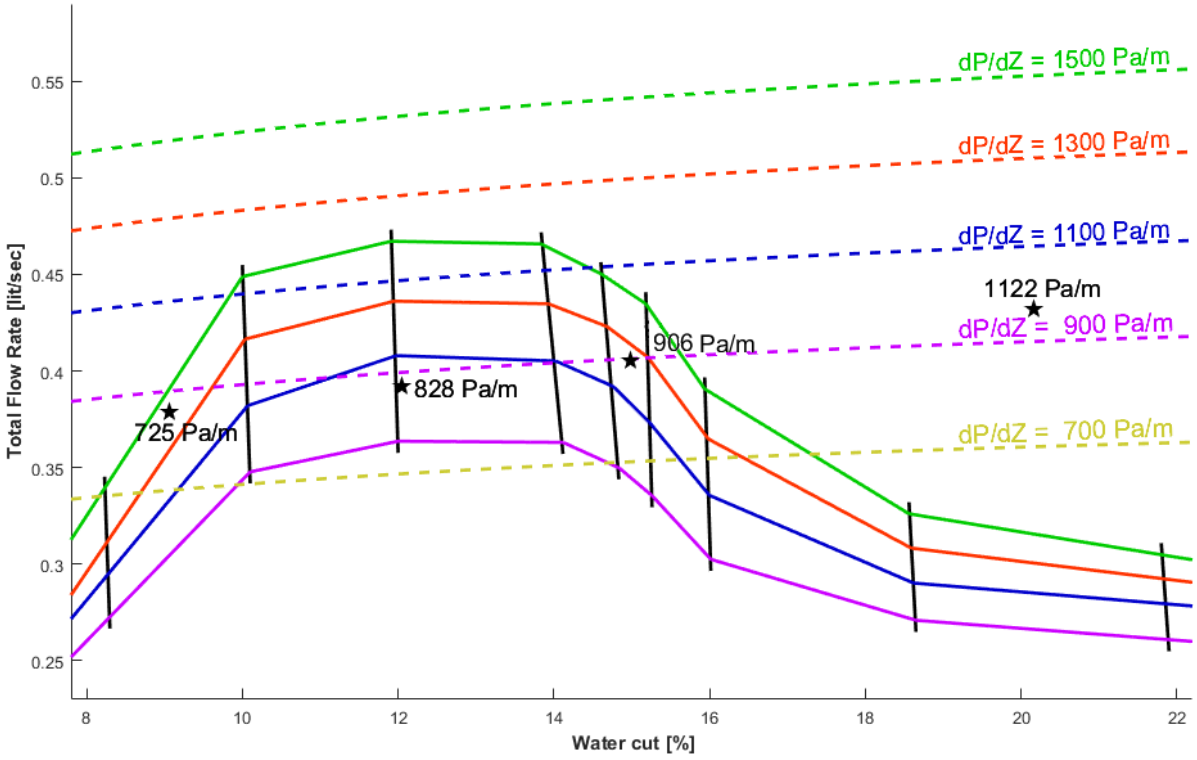

Figure 7.4: Numerical (solid lines), analytical (dashes lines) and experimental (black stars) results for a water cut range between 8% and 23%.

7.4. Velocity field comparison

In the previous section it was found that the numerical results above 14% start to deviate due to an incorrect length of the computational domain. The results below a water cut of 14% are however also deviating from the experiments. Therefore it is interesting to look at more quantities in the simulations like the velocity profiles. The velocity profiles for different simulations are shown in figure 7.5. In the first graph the velocity profiles of chapter 5 are also shown for a complete overview of all performed simulations. The velocity profile for 50°C is not displayed as stratified flow was found. On the left the complete velocity profile is shown and on the right a zoom in of the velocity profile of the oil core is shown.

From the velocity profile for 30°C it is seen that the oil core moves as a solid body through the pipe. The velocity across the whole core is constant. At a temperature of 20°C a small gradient is found at the oil core, and for the 40°C case even a bit larger. For 40°C there is a difference of around 0.08 m/s between the core center and the sides.

A large difference is seen between the holdup of 0.792 and the other two holdups. The total flow rate of this holdup is at the maximum of the pressure gradient contour lines in figure 7.1. The velocity profiles are a logical reflection of the different total flow rates. For the holdup of 0.697 the domain length was incorrect which resulted in a larger resistance and smaller velocities. Nearly constant velocities along the oil phase are again observed for the holdups 0.820 and 0.697. For the zoomed in figure of the holdup 0.792 again a velocity difference of 0.08 m/s is seen. While changing the pressure gradients for this holdup the profile shape is unchanged and only the absolute values differ. Between 900 and 1100 Pa/m a larger increase in velocity is found than between the other pressure gradients.

The velocity profiles of the experiments are not known. From the simulations a constant velocity profile is expected across the oil phase. For 40°C where the pressure loss became very high or at a holdup of 0.792 where a larger total flow rate was observed, small velocity gradients in the oil phase start to occur. The velocity differences are however still small.

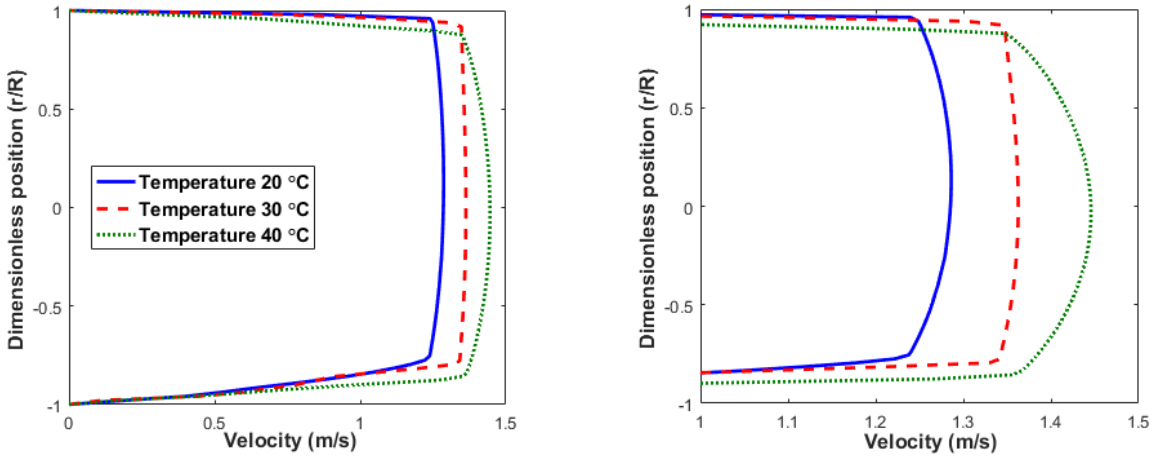

Figure 7.5: Velocity profiles for simulations I,II and III. Different temperatures for Ho=0.749 at a constant total flow rate of $0.430 \cdot 10^{-3} m^3/s$. Right figure is zoomed in at the oil core.

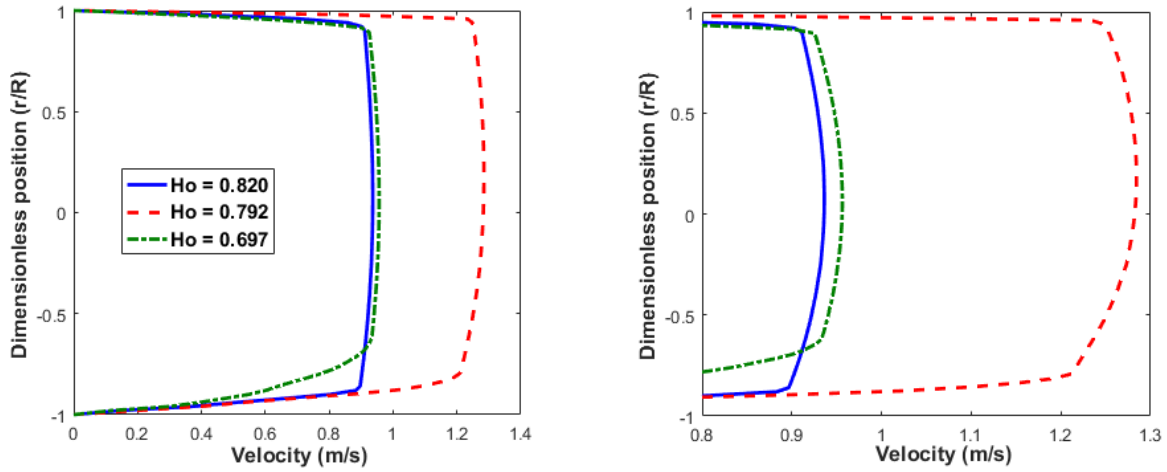

Figure 7.6: Velocity profiles for simulations V,VII and X. Different holdup fractions for a pressure gradient of 1100 Pa/m at 40°C. Right figure is zoomed in at the oil core.

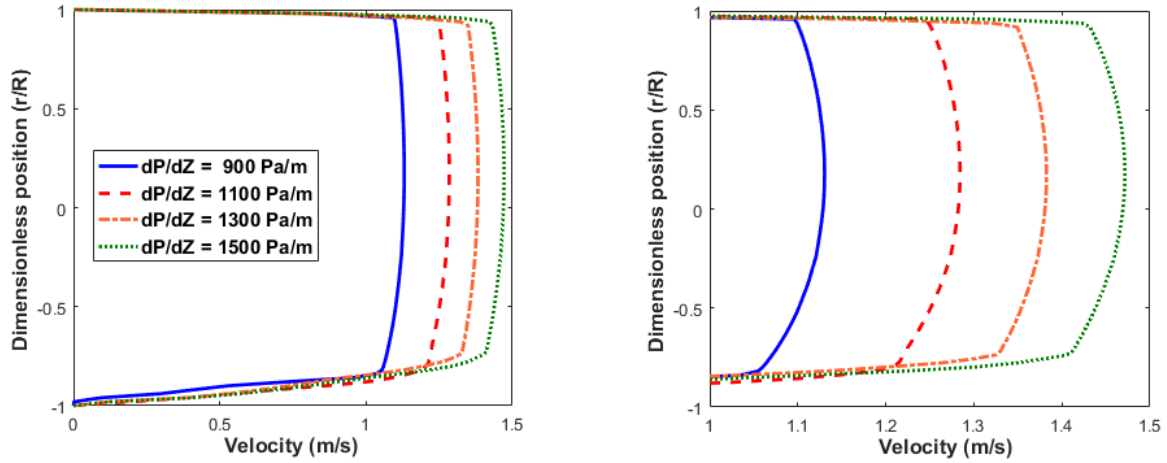

Figure 7.7: Velocity profiles simulations VI,VII,VIII and IX. Different pressure gradients for Ho=0.792 at 40°C. Right figure is zoomed in at the oil core.

7.5. Turbulence comparison

In chapter 5 the ratio of the turbulent and molecular viscosities was described as indication for the turbulence. A single phase water flow, at the same pressure gradient, has a ratio of around 95 which indicates that the flow is certainly turbulent. The ratios for core-annular flow were calculated between 19 and 30. For a temperature of 50°C the simulation converged to a stratified flow for which the ratio became approximately 95 again. Ratios of 14, 22 and 20 are found for the holdups of 0.820, 0.792 and 0.697, respectively. For the holdup of 0.792 no significant change in this ratio is observed for the different pressure gradients.

Figure 7.8 shows the turbulent kinetic energy and the non-dimensional turbulent kinetic energy. The simulation results are taken along a vertical line from the bottom to the top of the pipe. The data are representative values for the converged simulations. The figures are shown for the different temperatures of chapter 5, the different holdups and the different pressure gradients. The turbulent kinetic energy k is the mean kinetic energy of the turbulent fluctuations of equations 4.14,

$$k = \frac{1}{2}\left(\overline{u'^2} + \overline{v'^2} + \overline{w'^2}\right). \tag{7.1}$$

When solving the problem with the Reynolds Averaged Navier Stokes equations the fluctuations are not available as only the averaged velocities are solved. The turbulent kinetic energy is however solved with a transport equation of the $k-\epsilon$ model. The kinetic energy is made non-dimensional with the friction velocity $u^\star$ similar as in [16]. The $u^\star$ is calculated as in equation 4.20 with the water density and τ_w calculated from a force balance for a cylindrical pipe,

$$P_R \pi R^2 - P_L \pi R^2 = 2\pi R L \tau_w \quad \Rightarrow \quad \tau_w = \frac{\Delta P}{L}\frac{R}{2}. \tag{7.2}$$

At the wall the turbulent kinetic energy is low due to the damping effect of the wall. In the oil phase the values are low as expected due to the low Reynolds number. Close to the wall the highest intensities are obtained in the water phase. Some sharp peaks are observed but also some more flattened maxima are found. For 20°C most of the turbulence in indicated at the bottom and for 30°C and 40°C also some turbulence is indicated in the top water layer. For the different holdups some small differences are found. For the different pressure gradients the non-dimensional turbulent kinetic energy seems to be similar for all pressure gradients.

The numerical results for the high water cuts were found to be incorrect due to the short domain length but also the results below 14% water cut differ with the experiments. A still open question is how accurate the used turbulent model is for core-annular flow. The model is frequently used for single phase flow. For core-annular flow with a deformable interface the accuracy of the turbulent model is not yet known. Large eddy simulations or direct numerical simulations could be a suitable way to validate the low Reynolds k-ϵ model of Launder Sharma.

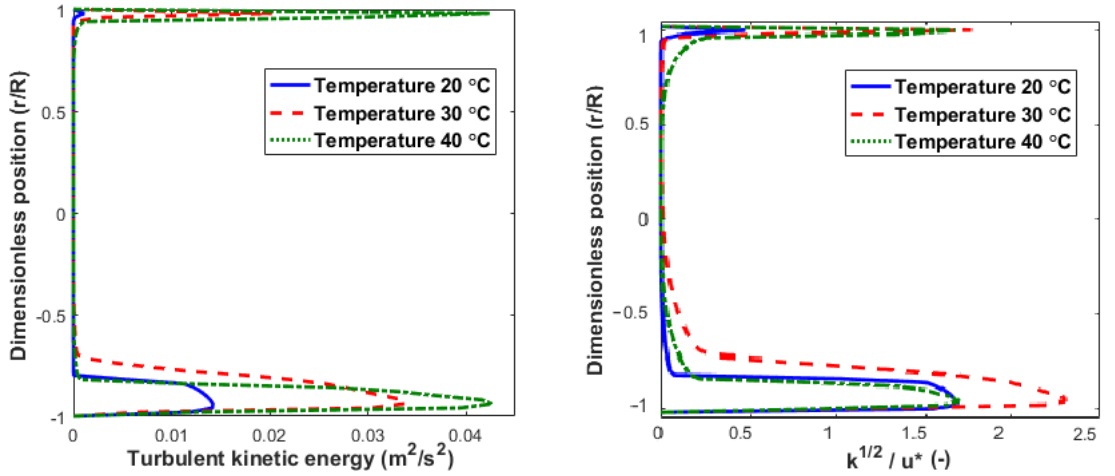

Figure 7.8: Turbulence properties for simulations I,II and III. Different temperatures for Ho=0.749 at a constant total flow rate of $0.430 \cdot 10^{-3} m^3/s$.

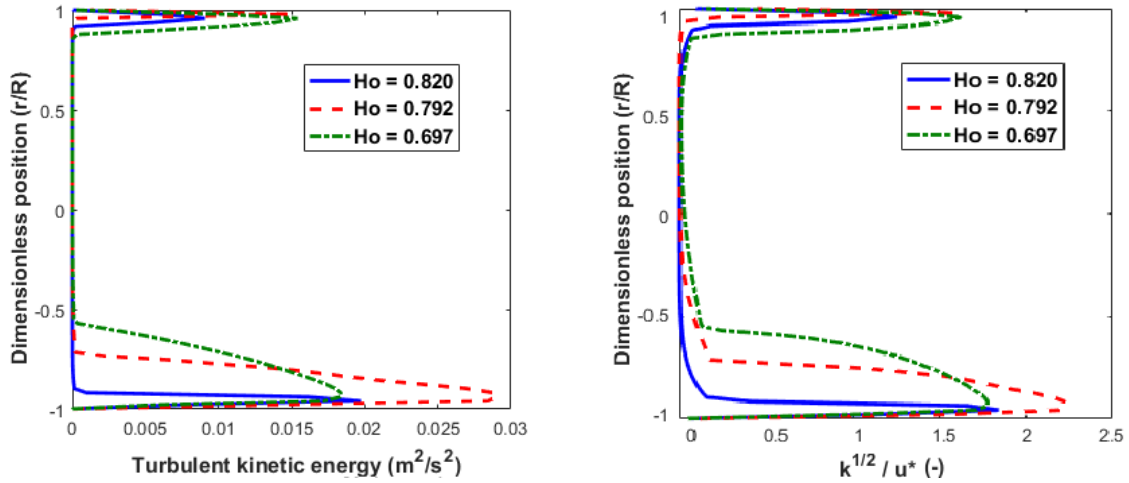

Figure 7.9: Turbulence properties for simulations V,VII and X. Different holdup fractions for a pressure gradient of 1100 Pa/m at 40°C.

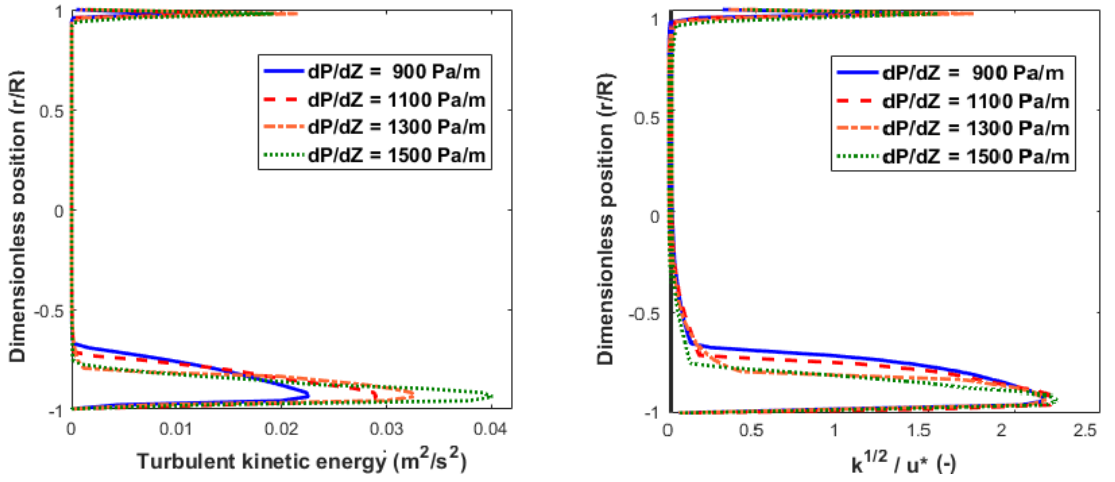

Figure 7.10: Turbulence properties for simulations VI,VII,VIII and IX. Different pressure gradients for Ho=0.792 at 40°C.

7.6. Conclusion

Simulation III from chapter 5 resulted in a water cut of 16.8%. The experiment to be reproduced has a water cut of 20%. To remove this deviation different initial holdup fractions are imposed in the simulations as described in this chapter. Through changing the oil holdups between 0.684 and 0.820 a range of water cuts is found between 8% and 22%. In addition to the experiment at 20% water cut, experiments were also conducted at water cuts of 9%, 12% and 15%. These experiments are used for additional comparison. Different pressure gradients are imposed and a solution grid is created with all the performed simulations. Linear interpolation is used to find the numerical pressure gradients and oil holdups for the similar water cut and flow rate values as the experiments.

The numerical and experimental techniques are compared with the analytical model of Ullmann & Brauner. The Ullmann & Brauner model is used to predict the oil and water flow rates for a prescribed pressure gradient at various values of the oil holdup fraction. A difference in behaviour between the numerical and analytical model is found. Above a water cut of 14% the difference is due to a wrong domain length in the numerical simulations. Below a water cut of 10% the difference is expected to be due to inaccuracies in both the Ullmann & Brauner model and the numerical simulations.

With the Ullmann & Brauner model, similar as with the numerical simulations, pressure gradients and oil holdups are predicted for the similar water cut and flow rate values as the experiments. The results of both the Ullmann & Brauner model and the numerical simulations are repeated here in table 7.5. It is found that for the pressure gradient the numerical simulations show large deviations. The Ullmann & Brauner model predicts the pressure gradient more accurately within 20% of the experimental measurements. At similar water cut the Ullmann & Brauner model predicts higher oil holdups than the numerical simulations.

Velocity profiles and profiles for the turbulent kinetic energy have been investigated for different temperatures, holdups and pressure gradients. Large velocity gradients are found in the water phase. For 40°C and for a holdup of 0.792 some small velocity gradients are found in the oil core. The other cases obtain a nearly constant velocity across the whole oil region. The turbulent characteristics indicate laminar flow in the oil core and possible turbulence in the water layer. Stronger turbulence is indicated at the bottom than at the top.

Table 7.5: Overview of experimental, analytical model and numerical results at 40°C (ν_O = 718 cSt).

	Water cut [%]	**Qtotal** $\cdot 10^{-3}$[m^3/s]	**Pressure gradient** [Pa/m]		**Oil holdup** [-]
Experimental	9.06	0.379	726		-
Ullmann & Brauner model	9.06	0.379	856	(18% error)	0.894
Numerical	9.06	0.379	1434	(98% error)	0.814
Experimental	12.04	0.392	829		-
Ullmann & Brauner model	12.04	0.392	872	(5% error)	0.860
Numerical	12.04	0.392	1028	(24% error)	0.792
Experimental	14.93	0.406	906		-
Ullmann & Brauner model	14.93	0.406	896	(-1% error)	0.828
Numerical	14.93	0.406	1240	(37% error)	0.745
Experimental	20.17	0.430	1122		-
Ullmann & Brauner model	20.17	0.430	964	(-14% error)	0.772
Numerical	20.17	0.430	-		-

8

Results from flow visualizations

Due to using periodic boundaries conditions the phase holdup in the simulation is fixed after initialization. A holdup ratio of 1.39 was used to initialize the phase holdup in chapter 5 and different phase holdups are investigated in chapter 7. The question is what the real phase holdup fractions are during the performed experiments. As part of his experimental study, van Duin also carried out a flow visualization with a high-speed camera. In this chapter a method is described to determine the phase holdup from these visualizations.

8.1. Numerical holdup

The flow in the experiments is recorded with a high-speed camera from the front and top view of the pipe. From the front view an average thickness of the water layer is obtained at the bottom and top interface. The left and right water layers are obtained from the top view visualizations. These images give four measurement points along the whole oil-water interface. Through these points a spline is fitted to obtain an estimate of the complete interface surface along the pipe perimeter. A spline is a function of piecewise polynomials which gives a smooth curve. With the area enclosed by this interface curve the phase holdup is estimated. As in reality the interface is irregular and not smooth the question is how accurate this method is.

For the numerical simulations of chapter 5 the same four points of the interface are obtained. Through these points also a spline is created for estimating the holdup. In the simulations, however, the real shape of the interface is known. The real phase holdup is compared with the spline holdup to find the accuracy of the method. On the left of figure 8.1 the four interface points of simulation II are indicated by blue dots. Through these points a spline is fitted, which is displayed by the blue line. The area enclosed by the spline is 74.13% of the full pipe area. The real oil holdup of the simulation is 74.94% which is a difference of 0.81%. As a reference also the real interface is included with the red curve, which can be compared with the spline.

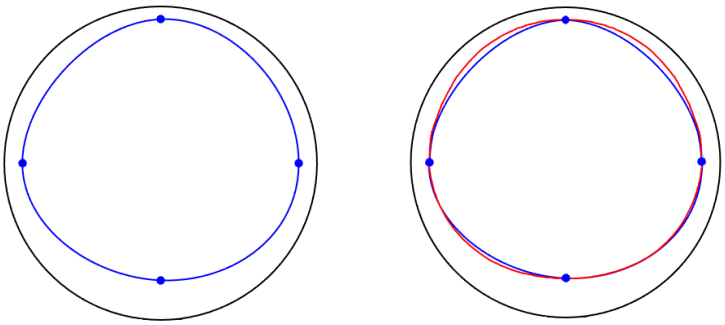

Figure 8.1: Interface estimation for simulation II. The blue line is a estimation of the interface and red line is the real interface.

Table 8.1 shows the results of six simulation cases to test the accuracy of the holdup estimation. Three simulations of chapter 5 are taken with four extra cases of chapter 7. Different holdups are tested with the last four extra cases. It is found that the oil holdup is mostly underestimated. When the core is concentric the real interface becomes close to a perfect circle making the spline more accurate. When the bottom interface raises this is mostly compensated with smaller water layers on the left and right side. This makes the interface less circular leading to a less accurate spline. The underestimation of the oil holdup fraction is found to be less than 0.01.

Equation 2.7, with a holdup ratio of 1.39, gives an oil holdup of 74.27% for the experimental flow rates. The oil holdup in the simulation is however 74.94%. This is the result of the control volumes size in the radial direction. All initial radii in one control volume are rounded off to the upper bound of the control size in the radial direction. In equation 2.7 an oil holdup of 74.94% corresponds to a holdup ratio of 1.34 for similar flow rates.

Table 8.1: Numerical comparison of real and spline holdup fraction.

Temp.	Initialization h	H_O Real	H_O Splines	Difference
20°C	1.39	0.7494	0.7447	-0.0047
30°C	1.39	0.7494	0.7413	-0.0081
40°C	1.39	0.7494	0.7498	0.0004
40°C	1.05	0.7919	0.7869	-0.0060
40°C	1.27	0.7641	0.7600	-0.0041
40°C	1.51	0.7235	0.7193	-0.0042
40°C	1.71	0.6963	0.6960	-0.0003

8.2. Experimental holdup

The visualizations for the temperatures 20°C to 50°C are processed for a water cut of 20%. For 40°C also the 12% water cut visualization is processed for comparison. From these visualizations grayscale images are obtained for the front and top view. In a grayscale image every pixel contains an intensity value which represents the amount of transmitted or reflected light. The intensity varies from black at the weakest intensity to white at the strongest intensity. Between black and white there is a range of gray shades varying between a value of 0 and 255. As oil has a high intensity and water a low intensity the phases can be distinguished. By choosing a proper grayscale threshold the interface between water and oil are tracked. The results are improved by enhancing the visualization such that the contrast between the phases is increased.

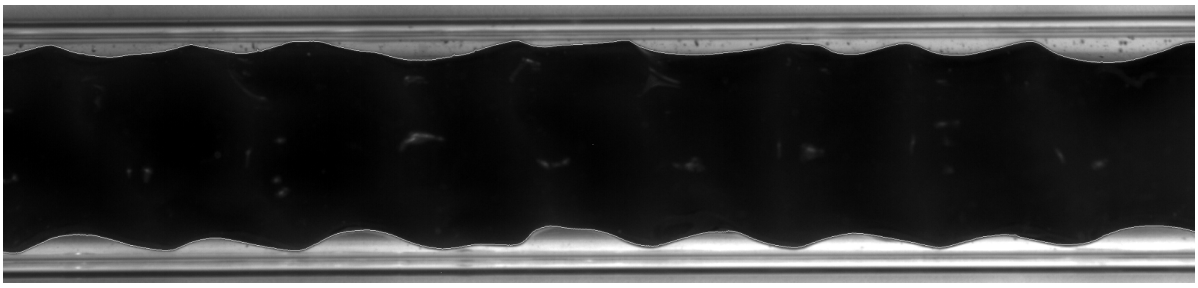

Figure 8.2: Front view of 30°C and 20% water cut. Interface estimation displayed with a white line.

Per experiment 1000 frames are captured corresponding to one second of flow. This corresponds with 1.25 meter based on the mixture velocity. For every frame the averaged height and amplitude are calculated from the number of pixels. The amplitude is taken as the largest vertical distance between a crest and a trough. These values are averaged over the 1000 available frames to obtain representative values of the experiments.

When the camera was focused it was not possible to get both views sharp in one image, although it was very close. This was because the aperture was far open for absorbing sufficient light, which

resulted in a small depth of field. This is probably also the reason for the different stripes in the area of the inner wall. In figure 8.2 the different grey stripes are well visible. It is therefore not entirely clear where the inner wall is located. Therefore, the outer wall of the pipe is used as a reference in the post-processing as this wall is better visible. Note that the diameter of the outer wall is 25 mm and the diameter of the inter wall is 21 mm. From the number of pixels covering the pipe outer diameter the pixels are converted to the SI unit of meters, and the thickness of the water layers and the amplitude sizes can be obtained. The results obtained from the data processing are summarized in table 8.2.

Table 8.2: Flow visualization results.

Experiment	**I**	**II**	**III**	**IV**
Temperature	20°C	30°C	40°C	40°C
Water cut	20%	20%	20%	12%
Water thickness Tw [-]				
Left	0.112	0.107	0.094	0.078
Right	0.126	0.124	0.114	0.096
Top	0.143	0.135	0.125	0.071
Bottom	0.153	0.174	0.181	0.120
Amplitude A^* [-]				
Left	0.115	0.101	0.117	0.064
Right	0.126	0.113	0.126	0.064
Top	0.157	0.121	0.121	0.078
Bottom	0.166	0.152	0.181	0.126
Ratio [-]				
Tw - Right/Left	1.13	1.16	1.21	1.22
Tw - Bottom/Top	1.07	1.29	1.45	1.68
A^* - Right/Left	1.10	1.11	1.07	0.99
A^* - Bottom/Top	1.06	1.25	1.50	1.62
Results [-]				
Oil holdup	0.749	0.748	0.749	0.836
Water holdup	0.251	0.252	0.251	0.164
Holdup ratio	1.34	1.35	1.34	1.43

The results for 50°C at a water cut of 20% are missing. In this experiment many oil droplets were present in the flow. These oil droplet often cross the interface on the visualization which makes it difficult to track the interface. The number of droplets on the interface were so high that these results are not reliable. For the other temperatures at a water cut of 20%, oil holdups of 74.8% and 74.9% are found. These values correspond to the imposed values of chapter 5 and correspond to a holdup ratio of 1.34 and 1.35. For the 12% water cut the oil holdup is 83.6% which corresponds to a holdup ratio of 1.43.

For the experiment I to III it is found that the eccentricity of the core is increasing for lower viscosities. At the top and bottom interface the linear dependency between the water layer thickness and the amplitudes are again found. Besides the expected eccentricity between the top and bottom there is also an unexpected eccentricity between the right and left side. Gravity is not playing a role in the horizontal direction so these water layers should logically be of equal width. A reason for this could be the limited depth of field in the flow visualization and because the top view was not perfectly in the focus. Another reason could be that the angle of the mirror for the top view was not perfectly 45 degrees. A ratio of 1.13 between the right and left water layers is the consequence of three pixels difference. A ratio of 1.21 is the consequence of five pixels difference.

8.3. Comparison of experimental and numerical results

In this section the holdup and wave characteristics of the flow visualizations are compared with the simulations results. For the holdup comparison also the analytical Ullmann & Brauner predictions are taken into account.

In table 8.3 the experimental, numerical and analytical oil holdups are shown. The 40°C results are repeated from table 7.5 and the results of 20°C are added. The Ullmann & Brauner model over predicts the oil holdup for all three cases with about 3%. The simulation for 20% water cut at 20°C, and thus also the other simulations from chapter 5, was initialized with exactly the same oil holdup as now found during the experiment. A difference of -5.3% is however found for the water cut of 12% at 40°C.

Table 8.3: Experimental, numerical and Ullmann & Brauner model estimations for the oil holdup at similar water cut and flow rate values.

	Temperature	Water cut	Qtotal	Oil holdup	
Experimental	20°C	20%	$0.430 \cdot 10^{-3}$ m^3/s	0.749	
Ullmann & Brauner model	20°C	20%	$0.430 \cdot 10^{-3}$ m^3/s	0.773	(3.2% error)
Numerical	20°C	20%	$0.430 \cdot 10^{-3}$ m^3/s	0.749	(0.0% error)
Experimental	40°C	12%	$0.392 \cdot 10^{-3}$ m^3/s	0.836	
Ullmann & Brauner model	40°C	12%	$0.392 \cdot 10^{-3}$ m^3/s	0.860	(2.9% error)
Numerical	40°C	12%	$0.392 \cdot 10^{-3}$ m^3/s	0.792	(-5.3% error)
Experimental	40°C	20%	$0.430 \cdot 10^{-3}$ m^3/s	0.749	
Ullmann & Brauner model	40°C	20%	$0.430 \cdot 10^{-3}$ m^3/s	0.772	(3.1% error)
Numerical	40°C	20%	$0.430 \cdot 10^{-3}$ m^3/s	-	

The wave characteristics of the experiment and numerical simulation for 20% water cut at 20°C are compared. Here the flow rates, viscosities, pressure gradients and the oil holdups are similar. For clarity the wave characteristics are repeated in table 8.4. In contrast to the almost concentric oil core in the experiment, a water layer thickness at the bottom of almost twice as large as at the top is found in the numerical simulation. The scaled water layers at the left and right side are a bit larger than the experiments but are in the same order of magnitude. The scaled amplitudes show the same behaviour as the water layers but the wave amplitudes are twice to five times as large in the experiment than in the numerical simulation.

8.4. Conclusion

The applied data processing method for the flow visualization results as described in this chapter is found to give accurate estimations of the holdups in the experiments. With this method oil holdups of 0.748 and 0.749 are found for the 20% water cut at different temperatures. These holdups corresponds to a holdup ratio of 1.34. At 40°C the oil phase up is 0.836 at 12% water cut which correspond to a holdup ratio of 1.43. It is found that the Ullmann & Brauner model slightly over predicts the oil holdup ratio by about 3%. The imposed holdups from chapter 5 correspond to the holdups of the experiments. Nevertheless only the 20°C simulation converged to the desired water cut of 20%. For this simulation all the key quantities are similar but a different eccentricity of the core is found and different wave amplitude sizes are found.

Table 8.4: Comparison of experimental and numerical interface results for 20°C at 20% water cut.

Simulation		**Experimental**	**Numerical**
Temperature		20°C	20°C
Oil viscosity	[cSt]	3338	3338
Water cut	[%]	20.02	19.9
Qtotal $\cdot 10^{-3}$	[m^3/s]	0.430	0.430
Pressure gradient	[Pa/m]	1004	951
Oil holdup	[-]	0.749	0.749
Water holdup	[-]	0.251	0.251
Water thickness Tw [-]			
Left		0.112	0.134
Right		0.126	0.131
Top		0.143	0.098
Bottom		0.153	0.186
Amplitude A^* [-]			
Left		0.115	0.050
Right		0.126	0.050
Top		0.157	0.034
Bottom		0.166	0.075
Ratios [-]			
Tw - Right/Left		1.13	0.98
Tw - Bottom/Top		1.07	1.90
A^* - Right/Left		1.10	1.02
A^* - Bottom/Top		1.06	2.17

9

Conclusions and recommendations

9.1. Conclusions

Computational fluid dynamics has been used in OpenFOAM to study core-annular flow through a horizontal pipe. The RANS equations are solved with the Launder & Sharma low-Reynolds number k-ϵ turbulence model. The simulations are quite expensive as the Courant number must be low for a correct modelling of the interface. Periodic boundary conditions are used to speed up the simulation process. The holdups are imposed in the simulations, using an estimate based on the finding of Bai et al. [29] that the holdup ratio is 1.39. In part of the simulations the flux imposed solver is used which retains the total flow rate constant; here the pressure gradient and water cut are obtained as output results from the simulation. In the other part of the simulations the pressure gradient solver is used, which means that the pressure gradient is imposed; here the total flow rate and the water cut are obtained as output results.

Numerical results are compared with experimental data of van Duin [1]. Numerical simulations are carried out with oil viscosities of 3338 cSt at 20°C to 383 cSt at 50°C at a water cut of 20%. The key quantities at 20°C are similar but for the higher temperatures (i.e. lower viscosities) wrong water cuts results were obtained. The different water cut values also led to differences between the numerical and experimental pressure gradients. At 50°C stratified flow was found in the numerical simulation in contrast to the core-annular flow pattern in the experiment.

An extensive study on the mesh dependence has been performed with the aim of reducing the simulation time. The number of control volumes in all directions has been tested. It is found that fine control volumes at the interface are required for correct results. Therefore the number of control volumes used at the interface can not be decreased. Nevertheless, the computer time could be reduced by taking coarser volumes in the center of the pipe, away from the interface. A decrease in computer time could also be obtained by switching from the flux imposed solver to the pressure gradient solver. It is found that the pressure gradient solver converges faster than the flux imposed solver.

Holdup variations are simulated for the 40°C case at an oil viscosity of 718 cSt. While varying the holdup, a range of water cuts are found between 8% and 23%. Four experiments are performed by van Duin in this water cut range which are used for validation. A grid of solutions is created by varying the imposed holdup and the imposed pressure gradient in the numerical simulations. With linear interpolation pressure gradients and oil holdups can be obtained from the simulation results for the four combinations of specific water cut and flow rates values for which experimental results are available. With this technique the numerical pressure gradients are compared with the experimental pressure gradients at similar water cuts and similar flow rates. However, differences of 24%, 37%, 98% are found at 40°C for a water cut of 12%, 15% and 9% respectively.

The experimental and numerical results at 40°C are compared with predications from the analytical

model of Ullmann & Brauner. Large differences are found between the numerical results and Ullmann & Brauner model below a 10% water cut and above a 14% water cut. The large difference above the water cut of 14% is due to an inaccuracy in the numerical simulations. The number of waves on the bottom dropped to only one above 14% water cut, which gives an increase in wave amplitude and therefore a decrease in total flow rate. The chosen domain length in the simulation may have a too large influence on the results if only a single wave is present. Below a water cut of 10% the difference is due to inaccuracies in both the Ullmann & Brauner model and the numerical simulations.

The holdups in the experiments are estimated from the flow visualizations which have been carried out by van Duin. The average thickness of the water layers are derived from four measurement points along the oil-water interface. Through these points a spline was fitted to obtain an estimate of the complete interface surface along the pipe perimeter. With the area enclosed by this interface curve the phase holdup was estimated. Oil holdup fractions of 74.8% and 74.9% at a water cut of 20°C were found. These holdups exactly match the holdups which have been imposed for the numerical simulations at different viscosities in chapter 5. Nevertheless, only the temperature 20°C case converged to a water cut of 20%.

9.2. Recommendations

Differences are found between the numerical results and the experiments. A reason for these differences could be due to the turbulence model. The k-ϵ model with the Lauder-Sharma constants are used. This model does not contain correction terms for the damped turbulence in the water layer close to the water/oil interface for core-annular flow. A Large eddy simulation would be an useful extension to this research to test the turbulence model.

In chapter 7 it is suggested that the simulations are influenced by the domain length. The influence of the chosen domain length for horizontal core-annular flow should be studied in more detail. In this respect it can be noted that the wave shapes are different for different viscosity and holdup values. Unfortunately, for larger domain lengths the simulation time will significantly increase. Some extra computational efficiency might be achieved by using a vertical symmetry plane in the longitudinal direction.

In the 20°C simulation from chapter 5 all the key quantities are similar to the experiment. The wave characteristics and eccentricity of the oil, however, are found to be different. A similar extension with holdups and pressure gradients variations as for the 40°C temperature would be very valuable for 20°C. The same applies for the 30°C and 50°C conditions.

At the end of Radhakrishnan's work the application solver was switched from the pressure gradient solver to the flux imposed solver. The advantage of the flux imposed solver is that it is more in common with the performed experiments. However, the flux imposed solver is not preferred due to the faster pressure gradient solver. A flux imposed solver where not the total flow rate is prescribed but the individual flow rates would be an improvement. This is because such a solver should not only prescribe the total flow rate but also the water cut, which is similar as in the experimental approach.

The numerical simulations at different temperatures are performed with the same surface tension. This assumption should be validated by measuring the surface tension of the oil which has been used during the experiments for different temperatures.

From the experimental flow visualizations a difference in the water layers are found between the left and right side of the pipe. As gravity only has influence vertically this difference is unexpected. New visualizations should be performed to study this difference more thoroughly. A more accurate technique to measure the thickness of the water film (e.g. by using conductivity probes) can also be considered. Furthermore a technique to determine the velocity profiles for the experiments could be very useful for validating the numerical simulations.

Bibliography

[1] H. J. van Duin, *Influence of oil viscosity on oil-water core-annular flow through a horizontal pipe,* Master of Science Thesis, Delft University of Technology. (2017).

[2] D. D. Joseph, R. Bai, K. P. Chen, and Y. Y. Renardy, *Core-annular-flows.* Annual Review of Fluid Mechanics, 29, pp: 65-90. (1997).

[3] IAPWS, *Viscopedia | a free encyclopedia for viscosity,* URL: http://www.viscopedia.com/viscosity-tables/substances/water/ (Accessed: 25-03-2017).

[4] J. C. Beerens, *Lubricated transport of heavy oil,* Master of Science Thesis, Delft University of Technology. (2013).

[5] E. M. R. M. Ingen Housz, *Experimental and numerical studies on core annular flows in a horizontal pipe,* Master of Science Thesis, Delft University of Technology. (2016).

[6] R. Radhakrishnan, *The effects of viscosity on core-annular flow.* Master of Science Thesis, Delft University of Technology. (2016).

[7] J. C. Beerens, G. Ooms, M. J. B. M. Pourquie, and J. Westerweel, *A comparison between numerical predictions and theoretical and experimental results for laminar core-annular flow.* American Institute of Chemical Engineers Journal 60, pp: 3046-3056. (2014).

[8] E. M. R. M. Housz, G. Ooms, R. A. W. M. Henkes, M. J. B. M. Pourquie, A. Kidess, and R. Radhakrishnan, *A comparison between numerical predictions and experimental results for core-annular flow with a turbulent annulus.* International Journal of Multiphase Flow, 95, pp: 271-282. (2017).

[9] G. Ooms, *Fluid-mechanical studies on core-annular flow.* PhD Thesis, Delft University of Technology. (1971).

[10] R. V. A. Oliemans, *The lubricating-film model for core-annular-flow.* PhD Thesis, Delft University of Technology. (1986).

[11] G. Ooms, C. Vuik, and P. Poesio, *Core-annular flow through a horizontal pipe: Hydrodynamic counterbalancing of buoyancy force on core.* Physics of Fluids, 19: 092103. (2007).

[12] R. V. A. Oliemans, G. Ooms, H. L. Wu, and A. Duijvestijn, *Core-annular oil/water flow: the turbulent-lubricating-film model and measurements in a 5 cm pipe loop.* International Journal of Multiphase Flow, 13, pp: 23-31. (1987).

[13] J. H. Ferziger and M. Peric, *Computational Methods for Fluid Dynamics*, Springer. (2002).

[14] F. Moukalled, L. Mangani, and M. Darwish, *The Finite Volume Method in Computational Fluid Dynamics*, Springer. (2016).

[15] D. C. Wilcox, *Turbulence modeling for CFD*, DCW Industries. (2006).

[16] F. Nieuwstadt, B. Boersma, and J. Westerweel, *Turbulence, Introduction to Theory and Applications of Turbulent Flows*, pp: 133. Springer. (2016).

[17] J. Brackbill, D. Kothe, and C. Zemach, *A continuum method for modeling surface tension,* Journal Computational Physics, 100, pp: 335-354. (1992).

[18] S. S. Deshpande, L. Anumolu, and M. F. Trujillo, *Evaluating the performance of the two-phase flow solver interfoam.* Computational Science and Discovery 5(1): 014016. (2012).

[19] C. Kouris and J. Tsamopoulos, *Dynamics of axisymmetric core-annular flow in a straight tube. i. the more viscous fluid in the core, bamboo waves.* Physics of Fluids 13, pp: 841-858. (2001).

[20] C. Kouris and J. Tsamopoulos, *Dynamics of axisymmetric core-annular flow ii. the less viscous fluid in the core, saw tooth waves.* Physics of Fluids 14, pp: 1011-1029. (2001).

[21] J. Shi, *A study on high viscosity oil-water two phase flow in horizontal pipes.* PhD Thesis. Cranfield University. (2015).

[22] O. M. H. Rodriguez and A. C. Bannwart, *Analytical model for interfacial waves in vertical core flow.* Journal of Petroleum Science and Engineering, 54, pp: 173-182. (2001).

[23] P. A. M. Boomkamp, *Stability of parallel two-phase flow,* PhD Thesis, University of Twente. (1998).

[24] A. Ullmann and N. Brauner, *Closure relations for the shear stress in two-fluid models for core annular flow.* Multiphase Science and Technology, 16, pp: 335-387. (2004).

[25] D. D. Joseph and Y. Y. Renardy, *Fundamentals of Two-Fluid Dynamics, Part I: Mathematical Theory and Applications.*, Interdisciplinary Applied Mathematics. Springer-Verlag. (1993).

[26] D. D. Joseph and Y. Y. Renardy, *Fundamentals of Two-Fluid Dynamics, Part II: Lubricated Transport, Drops and Miscible Liquids*, Interdisciplinary Applied Mathematics. Springer-Verlag. (1993).

[27] Y. Li, J. Renardy, *Direct simulation of unsteady axisymmetric core-annular flow with high viscosity ratio,* Journal of Fluid Mechanics, 391, pp: 123-149. (1999).

[28] R. Bai, K. Kelkar, and D. D. Jospeh, *Direct simulation of interfacial waves in a high viscosity ratio and axisymmetric core annular flow,* Journal of Fluid Mechanics, 327, pp: 1-34. (1996).

[29] R. Bai, K. Chen, and D. D. Jospeh, *Lubricated pipelining: Stability of core-annular flow v: Experiments and comparison with theory,* Journal of Fluid Mechanics, 240, pp: 97-132. (1992).

[30] E. group, *The open source cfd toolbox,* URL: http://www.openfoam.com/documentation/ .